Chapter 2
Coastal Oceanography, Geology, and Biology

2.1 The Coast as Acoustic Waveguide

From the viewpoint of low- and mid-frequency shallow water acoustics, the ocean shelf is a waveguide, limited by a pressure release boundary above (the ocean's surface) and an absorbing boundary below (the ocean bottom/seabed). In describing the sound field radiated from a source (whether point or distributed), both the waveguide's interior and boundaries play an essential role. To describe this waveguide's interior and boundaries, we must delve into the areas of coastal physical oceanography, geology and geophysics, and biology. These areas are vast scientific fields on their own, and so we limit ourselves here to touching on only the elements of them that are most germane to shallow water acoustics. The rest we leave to the reader to explore independently. Toward this, we initially provide three physical oceanography references, which should give the reader a starting point: Pond and Pickard (1983); Bowden (1983); and Cushman-Roisin (1994). We will start by looking in the first six sections of this chapter (Sects. 2.1–2.6) at physical oceanography, then devoting Sects. 2.7–2.10 to marine geology, and finally ending in Sect. 2.11 with some discussion of marine biology.

In looking at the shallow water acoustic waveguide in general, the sound speed in both the water and the bottom depends mainly on depth (the z coordinate) and as a "beginners rule" varies slowly in the horizontal coordinates and in time (more precisely, geotime). Thus, it is commonly taken that the sound-speed field $c(x, y, z)$ is to first order only a function of z. This allows us to look initially at the vertical variability of the sound speed at different geographical locations and seasons and make both sensible intercomparisons and distributions of variability.

In that vein, distilled results of different observations and measurements of sound-speed profiles in various areas of the world ocean are shown in Fig. 2.1. We can see that the water column sound-speed profiles differ depending on geographical location and season, whereas the seabed sound-speed profiles are more simply determined by depth (overburden pressure) and material composition. We will attempt to explain the details of these profiles in the sections that follow.

B. Katsnelson et al., *Fundamentals of Shallow Water Acoustics*,
The Underwater Acoustics Series, DOI 10.1007/978-1-4419-9777-7_2,
© Springer Science+Business Media, LLC 2012

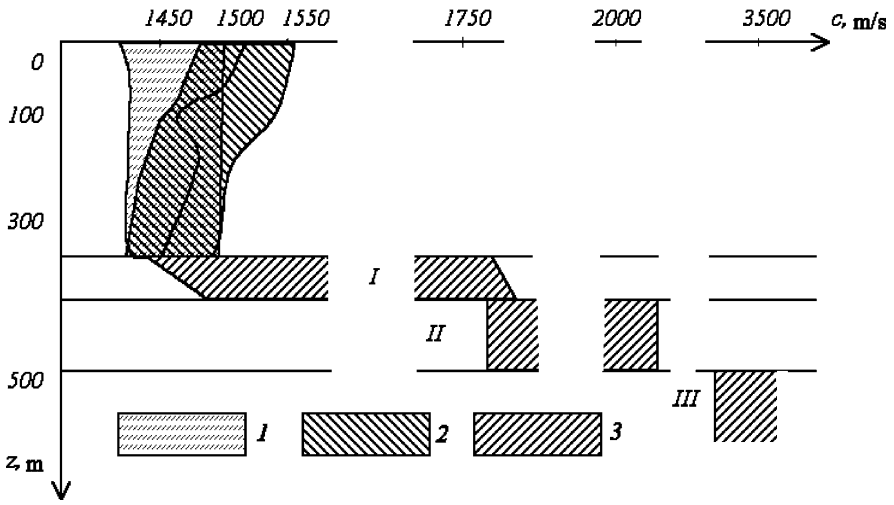


Fig. 2.1 Sound-speed profiles in different areas of the world's coastal ocean and for different seasons. 1 – higher latitude, winter sound-speed profiles, 2 – lower latitude year round and summer mid-latitude profiles. 3 – bottom sound speed. The nonmonotonic curve included shows a sound-speed profile with a possible pure refraction duct

For analytical calculations and estimation, we can select a small numbers of "canonical" (i.e., generic or typical) sound-speed profiles that can be used to characterize a large fraction of the shallow water environment (Kuperman and Lynch 2004). However, these profiles, shown in Fig. 2.2, are merely first-order simplified representations of the reality of the shallow water seas (as represented by Fig. 2.1). In order to know when they can be used or when they should be augmented, we must first discuss the real environment. We will do that next, approaching the coastal oceanography first, and then moving to the coastal marine geology.

2.2 Properties of Sea Water: Vertical Stratification and Its Seasonal Variability

To a good approximation, we can consider seawater as a two-component medium, consisting of a solvent (water) and various salts. The concentration of salt (salinity) is usually denoted as S and is measured in pro-mille (denoted as ‰) or in parts per thousand (ppt). The average value of salinity in deep ocean seawater is about 35‰. Variations of salinity within the shelf zone are in the order of 20–35 ppt.

The thermodynamic state of sea water is characterized by temperature T°, density ρ, salinity S, and pressure P and is described by the state equation

$$\rho = \rho(T^\circ, S, P). \tag{2.1}$$

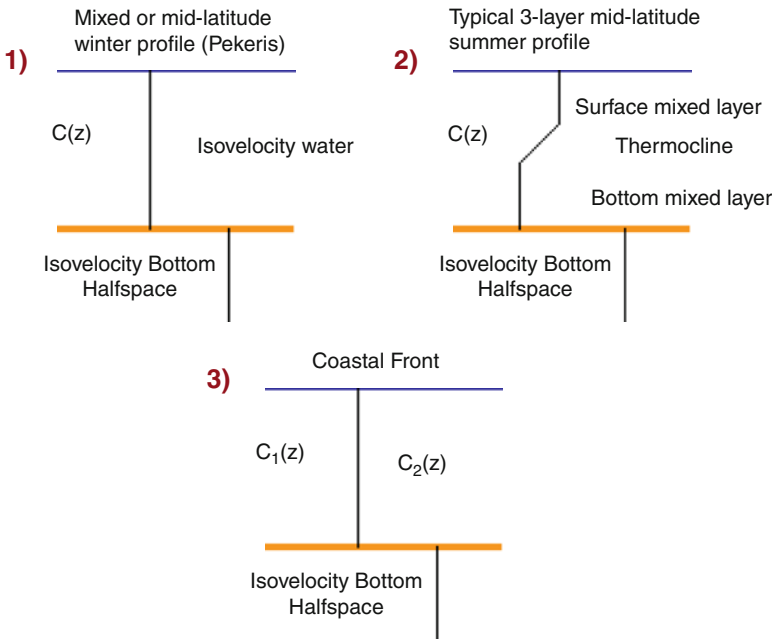


Fig. 2.2 Three simple sound-speed profiles which characterize much of shallow water acoustics. The first profile is the so-called "Pekeris waveguide," typical of mixed water column conditions over a simple bottom. The second profile is the "three-layer model," typical of low-latitude or summer mid-latitude waters over a simple bottom. The third profile is that of an enormously simplified coastal front, again over a simple bottom

Due to the complexity of the composition of seawater, this equation can be written only empirically. In physical oceanography, the parameters temperature, salinity, and pressure are basic, whereas other observed characteristics (sound speed, heat capacity, conductivity, etc.) are expressed through these three parameters. As is well known, these parameters depend on both space and time (we will denote this "slow" time as geotime, T, in contrast with the "fast" time, t, used in forming expressions for the high-frequency oscillations of the wave fields).

One of the main characteristics of seawater is its bulk adiabatic compressibility (defined by the relative variation of the density with pressure)

$$\beta_a = \frac{1}{\rho}\left(\frac{\partial \rho}{\partial P}\right)_a \tag{2.2}$$

which also depends on the basic thermodynamic parameters and, in relating it to acoustics, generally depends on the frequency of the pressure oscillations (of sound) as well. The sound speed is connected to β_a by $c = 1/\sqrt{\rho\beta_a}$. In our case, $\beta_a \sim 4 - 5 \times 10^{-10}\,\mathrm{Pa}^{-1}$. β_a depends on T° and S, and according to experimental data (e.g., Babii 1983), compressibility decreases with both increasing temperature and salinity, whereas sound speed correspondingly increases.

Table 2.1 Coefficients of equation of state

β_a [Pa^{-1}]	β_T [$°K^{-1}$]	$\beta_S(\circ/\circ\circ)^{-1}$	$\partial c/\partial T$[m s^{-1} $°K^{-1}$]	N [cph]
$4-5\times10^{-10}$	1.3×10^{-4}	8×10^{-4}	4.6	<10

This variability of β_a determines the dependence of the sound speed upon the thermodynamic parameters; of particular importance, the dependence of the sound speed on temperature goes as $\frac{\partial c}{\partial T^\circ} \sim 4.6$ m/(s degree), as a rough "rule of thumb."

We also need to define the thermal expansion coefficient

$$\beta_T = -\frac{1}{\rho}\left(\frac{\partial \rho}{\partial T^\circ}\right)_{S,P} \tag{2.3}$$

and the coefficient of variation of the density as a function of salinity

$$\beta_S = \frac{1}{\rho}\left(\frac{\partial \rho}{\partial S}\right)_{P,T}. \tag{2.4}$$

With these quantities defined, we can then write down the differential equation of state of seawater as

$$\frac{d\rho}{\rho} = \beta_T dT^\circ + \beta_a dP + \beta_S dS \tag{2.5}$$

where (typical) numerical values of the coefficients are shown in the Table 2.1 and N is the Brunt–Vaisala frequency (see Appendix A). This result will be used in our further work.

Temperature variability is a good first-order proxy for sound-speed variability in shallow water, since the well-known equation of state (Urick 1975) gives that the sound speed is approximately

$$c = 1449.2 + 4.623T^\circ - 0.0546(T^\circ)^2 + 1.391(S-35) + 0.017z \tag{2.6}$$

where c is in m/s, T° is in degrees Celsius, S is salinity in ppt or psu, and z is in meters. Since depth effects only add about 0.017 s^{-1} to this equation, they are often ignored to first order in shallow water. Salinity also is a generally weak sound-speed signal (though not always, as coastal waters show the largest variation in S). For the range of T° and S typically found in coastal waters ($T^\circ \sim$ 6–25°C and $S \sim$ 20–35 ppt), it is easily seen that temperature effects dominate. However, to get at the temperature field theoretically, the physical oceanographer has to consider the salinity just as much as the temperature, since the density field is the most critical parameter in ocean flows and structure, and density is about equally dependent on temperature and salinity effects. Thus, (2.5) is the critical state equation for physical oceanography, whereas (2.6) is the important state equation for ocean acoustics.

The temperature distribution in the shallow water column is determined by both the large-scale water masses found at a particular location and the competition between solar heating, medium stratification and vertical mixing, the latter of which is induced by wind stress on the surface as well as wave and current stress on the bottom. In modeling the vertical temperature distribution, we will consider here a simple yet physical and useful model, published by James (1977), which is also described in the coastal oceanography textbook by Bowden (1983). This variability in the vertical temperature profile with geotime, i.e., the function $T^{\circ}(z, T)$, is central to shallow water acoustics.

We begin with the one-dimensional vertical diffusion equation for temperature,

$$\frac{\partial T^{\circ}}{\partial T} = \frac{\partial}{\partial z}\left(K_z \frac{\partial T^{\circ}}{\partial z}\right), \tag{2.7}$$

where T is the geotime and K_z is the vertical eddy diffusion coefficient of heat, dependent on depth and geotime. To take into account that mixing is inhibited by density stratification/stability, K_z is modified to

$$K_z = K_0(1 + \sigma Ri)^{-p}, \tag{2.8}$$

where $g' = K_0 g$ is the coefficient for neutral stability (no stratification present) and Ri is the gradient Richardson number, given by

$$Ri = g\beta_{\mathrm{T}} \frac{\partial T^{\circ}}{\partial z} \Bigg/ \left(\frac{\partial U}{\partial z}\right)^2. \tag{2.9}$$

In (2.8) and (2.9), σ, p are empirically determined constants, on the order of $\sigma = 0.3$ and $p = 1.5$, respectively; U is the horizontal current magnitude; and β_{T} is the coefficient of thermal expansion of water.

The solution of (2.7) is subject to surface and bottom boundary conditions.

At the surface,

$$\left[K_z \frac{\partial T^{\circ}}{\partial z}\right]_{z=0} = \frac{\tilde{Q}}{\rho c}, \tag{2.10a}$$

where $\tilde{Q}$ is the flux of heat downward through the surface (in particular, the average heat flux from the Sun is about 0.14 W/cm^2). At the bottom, the turbulent diffusion of heat is inhibited, so

$$\left[K_z \frac{\partial T^{\circ}}{\partial z}\right]_{z=H} = 0. \tag{2.10b}$$

The temperature gradient, $\partial T^{\circ}/\partial z$, is then determined via calculation. The heat input $\tilde{Q}$ and the wind speed are the meteorological inputs to the model (the wind

speed being one of the factors in K_z, as we will see). The term $(\partial U/\partial z)^2$ in (2.9) is obtained by assuming that the bottom and surface boundary layers have logarithmic velocity profiles, the surface one caused by the wind stress and the bottom one caused by the tidal currents. For instance, the near-bottom velocity profile will look like

$$u = \frac{u_*}{k_0} \ln \frac{z}{z_0}, \tag{2.11}$$

where z is the distance from the bottom, $u_* = (\tau/\rho)^{1/2}$ is the so-called friction velocity (τ being the stress due to the near-bottom tidal current), z_0 is a roughness parameter, and k_0 is von Karman's constant, approximately equal to 0.4. A similar form is easily found in the literature for the surface boundary layer. This form will be familiar to many readers as the "law of the wall."

The neutral eddy diffusivity (at $Ri = 0$) is expressed as the sum of surface and bottom parts as well, i.e.,

$$K_0 = K_{0\mathrm{W}} + K_{0\mathrm{T}} \tag{2.12}$$

where $K_{0\mathrm{W}}$ is proportional to the wind speed and $K_{0\mathrm{T}}$ is proportional to the tidal current speed and the depth of the water.

With all this in hand, the model is run. When a thermocline is formed at a certain depth, $z = z_0$, it is assumed that wind mixing cannot penetrate below that depth and that bottom (tidal current) mixing cannot penetrate above it. Moreover, as is also usual in mixing models, if $\partial T^\circ/\partial z$ becomes positive, indicating unstable stratification, the model mixes the temperature instantaneously over a range of depth, thus restoring stability to the profiles. By integrating (2.7) numerically, starting from given initial conditions, one can compute the evolution of the temperature profile with time, and indeed James' results look exactly like our three-layer model of shallow water, i.e., a surface layer, a thermocline, and a bottom mixed layer, as seen in Fig. 2.3.

We should make two notes about the temperature stratification model presented above, particularly from the viewpoint of an acoustics "model user." First, and most importantly, while this model is useful for understanding the physics of how the surface mixed layer, bottom mixed layer, and thermocline arise, it is relatively weak for predictive use. Mixed layer models are demanding in their inputs for wind stress, insolation, initial stratification, etc., and typically, this much detailed input is hard to get. For acoustics users, climatology probably gives a good enough first-order estimate of stratification, and an in situ XBT or CTD gives the best improvement to that. Second, the model discussed above is one of the simpler ones, and more complicated models do exist which include salinity effects, more detailed models of turbulence and mixing, and even three dimensions. We refer the reader to the classic article by Price et al. (1986) as an example of a more sophisticated 1D approach.

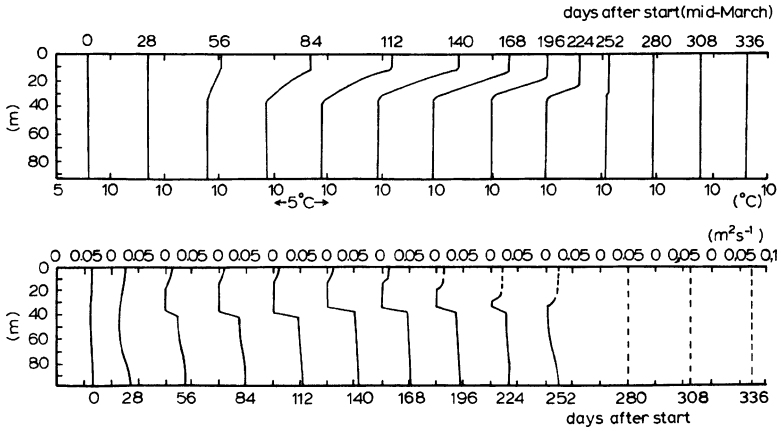


Fig. 2.3 Development of a seasonal thermocline, computed from the 1D model discussed. *Top panel* shows temperature profiles at 28-day intervals, the *bottom panel* the corresponding coefficients of eddy diffusion at the same times. With permission from I.D.James, Estuar. Coastal. Mar. Sci, 7, 197–202. Copyright Academic Press (London) Ltd

Extension of the shelf sound-speed profile results to the slope is straightforward, at least to first order. One just gets rid of the bottom mixed layer in the shelf profile, and extends the downward refracting gradient layer to the typical downward refraction one gets in the first kilometer depth due to the exponential temperature decrease, using the climatology of the region as a guide. This gives the profile shown in Fig. 2.3 top panel. However, this is a generic mean profile and does not include the effects of fronts, eddies, IWs, fine structure, etc. These are often present on the slope, and so the above "prescription" must be used with extreme care.

One also notes that down to the depth of about 750 m, the depth of the mid-latitude deep sound channel axis, this profile is downward refracting. This means that sound coming off the shelf onto the slope will "hug the bottom," giving high sound levels near the bottom, and a shadow zone just above that. However, past the depth of 750 m (it often can be down to ~1 km), the sound will no longer be driven into the bottom, but rather the field will "lift off" the bottom and continue its travel in the well-known deep ocean SOFAR axis. This can be modified by the shelf break front and other structure; so again, one must look at this effect exercising care.

2.3 Horizontal Stratification and Its Variability: Fronts and Eddies, Surface Ducts, and Storm Surges

In the above discussion, we concentrated on the vertical variability of the temperature field and discussed a simple model of how that variability arises. This vertical structure is the most important feature of the shallow water column, as the water column and bottom are approximately horizontally stratified (comprised of

vertically stacked layers) over the propagation scales of interest, which reach to about 50 km in shallow water. However, horizontal stratification is a broad-brush first approximation only, and in many shallow water scenarios, there is appreciable sound-speed variability in the horizontal direction, as well as in the vertical. Perhaps the strongest horizontal variability in shallow water is due to shallow water fronts, and so we address that topic next.

There are four separate kinds of shallow water fronts which are of potential interest to underwater acousticians. They are (1) upwelling fronts, (2) tidal mixing fronts, (3) buoyant plume fronts, and (4) shelf break fronts. These fronts all have somewhat different dynamics and characteristics, which in turn determine what type of horizontal temperature/sound-speed gradients they produce and where on the continental shelf they are observed. We will look at all four of these fronts and present examples where possible.

Upwelling fronts. Upwelling of water at the coasts is a very well-known phenomenon, particularly since it has a profound effect on fishing activity, the Peruvian anchovy fisheries being perhaps the most famous example (Bowden 1983). Specifically, upwelling is the process whereby cool water from depths on the order of 50–300 m is pumped upward into the surface layer due to the effect of wind, thereby bringing nutrient salts into the photic regions near the sea surface. From the point of view of acoustics, the biologically important transport of salts to the surface (a salinity signal) is almost irrelevant; however, the transport of cold, deep water to the normally warm surface layer is not, as this temperature signal provides an appreciable sound-speed signal, and indeed an acoustic "front."

Physically, upwelling is caused by two things: the first is the wind-induced Ekman transport of near-surface water away from the coast (surface Ekman transport being produced by the balance between the wind stress and the Coriolis force). The second is the continuity equation demanding that the amount of (warm) surface water that gets transported seaward must be replaced with an equal amount of deeper (cold) water being transported shoreward and eventually to the surface, so as to balance the masses. Ekman transport is to the right of the wind in the Northern Hemisphere and to the left of it in the Southern Hemisphere, so the direction of the wind along the coast is critical. We should note that if the wind direction is such that it is pushing the warm surface waters onshore, rather than offshore, an analogous process called downwelling occurs. This pushing of warm water onshore tends to create a deeper surface warm layer near the coast, rather than a sharp front. The basic mathematics of both the Ekman transport and the continuity equation are to be found in numerous elementary oceanography textbooks, and we would refer the reader to the treatments by Bowden (1983) and Cushman-Roisin (1994) for details.

Though one should use a more exact dynamical model to construct the geometry of an upwelling front, we can create a first-order estimate of upwelling frontal structure useful for acoustics from rather simple dynamics. In the top and bottom panels of Fig. 2.4, we show a two-layer ocean before and after an upwelling event, with the initial warm surface layer being of depth H, density ρ_1, and sound speed c_1. This layer overlies a (mathematically) infinitely deep layer with density ρ_2 and

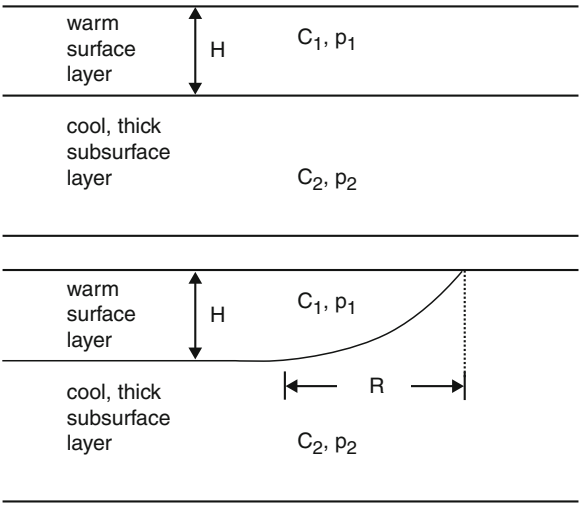


Fig. 2.4 *Top panel* shows the two-layer system of warm surface layer overlying a deep cooler layer near the coast. *Lower panel* shows result of upwelling, where deep cooler water is brought up to the surface due to the warmer surface layer being pushed seaward. The distance R over which the front extends is a good dynamic approximation, but the exact shape of the front needs a more exact dynamical treatment to determine – our figure above is an "artist's conception" in that respect

sound speed c_2. After upwelling occurs, the cold lower layer rises from depth H to the surface over a distance R, which is given by Cushman-Roisin (1994) as

$$R = (g'H)^{1/2}/f_C, \tag{2.13}$$

where

$$g' = \frac{(\rho_2 - \rho_1)}{\rho_2} g \tag{2.14}$$

is the "reduced gravity" (see Appendix A.3) and

$$f_C = 2\Omega_E \sin\theta \tag{2.15}$$

is the so-called Coriolis parameter, where Ω_E is the rotational rate of the earth and θ is the latitude. Thus, one has a horizontal sound-speed gradient which is sharp across the surface layer, and has a depth average value (over the layer depth) of $(c_1 - c_2)/R$. Here, R is typically on the order of 5–10 km, and Δc is of the order 10–50 m/s so that the average horizontal gradient is of the order 1–10 m/s/km or $10^{-3} - 10^{-2}\,c^{-1}$. This is an appreciable horizontal gradient for acoustics.

Tidal mixing fronts. Whether or not a thermocline develops in the late spring or early summer depends critically on whether or not there is enough turbulent kinetic energy generated throughout the water column to mix heat downward at the rate at which it is being received at the surface. Both surface winds and tides can create turbulence and mixing, but the winds are an intermittent mechanism, whereas the tides are a constant one. Thus, we will consider here the case where the mixing is due to tides alone.

From a rather simple derivation (Bowden 1983), one can show that there is complete vertical mixing of the water column when

$$\frac{H}{U_t^3} \sim 70 - 100 \,\text{per}\,\text{m}^{-2}\,\text{s}^{-3}, \tag{2.16}$$

where H is the water column depth in meters and U_t is the tidal current speed in m/s. This form easily lets us see the depths to which one expects full mixing. Taking U_t equal approximately to 0.5–0.7 m/s (about one to one and one-half knots) as typical tidal current magnitudes, full mixing will be seen in water columns with depths between ~10 and 35 m. Past this point, a two (or more)-layer system will evolve. For water depths greater than this mixing depth, the lower layer will be at some sound speed c_{mixed}, whereas above the mixed region, the water sound speed will be c_{upper} (in the two-layer model). This idealized system agrees well with real world measurements of this effect, as shown by comparing our simple model with data, as seen below (Bowden 1983), in Fig. 2.5.

Buoyant plume fronts. River outflow plumes create fronts that are well known to even lay observers, as large river discharges after storms often contain copious amounts of mud and fine sediment, which show the edges of the plume sharply against the much clearer, deeper water. However, these plume fronts are not as acoustically strong as the other three types, for reasons we now discuss. The main signal of a buoyant (freshwater) river plume front is salinity, which may be ~20–30 ppt compared to 35 ppt in the deep ocean. This creates up to an ~15–20 m/s sound-speed contrast between the buoyant plume and its surroundings, a not insignificant disturbance. However, these strong salinity signals only extend over the top meter or two of the water column near their origin. These plumes then travel many tens of kilometers outside the river mouth, and the initial freshwater pulse is spread out both horizontally (by wind and currents) and vertically (by mixing), thus diluting it. By the time river salinity signals have traveled an appreciable distance, the sound-speed disturbance is only 5 m/s or less. This is weak as far as coastal horizontal fronts are concerned. However, the near-surface acoustic duct that they can create can be very effective in ducting sound at higher frequencies, as we will discuss later in our section on surface ducts.

Shelf break fronts. If the buoyant plume fronts are the least important ones to acoustics, their distant offshore cousins, the shelf break fronts, are perhaps the most important. The shelf break regions of the world (the lines where the continental shelves dip abruptly into the continental slopes, usually at depths of 100–200 m) are often the boundaries between very cool (but somewhat fresher) coastal waters and very warm (but somewhat saltier) deep waters influenced by large boundary current systems such as the Gulf Stream and Kuroshio. An example of a well-measured shelf break front from the 1996 PRIMER experiment (Gawarkiewicz et al. 2004; Sperry et al. 2003) is shown in Fig. 2.6. This front obviously has a lot of structure, unlike our simple cartoon in Fig. 2.2(3), and serves

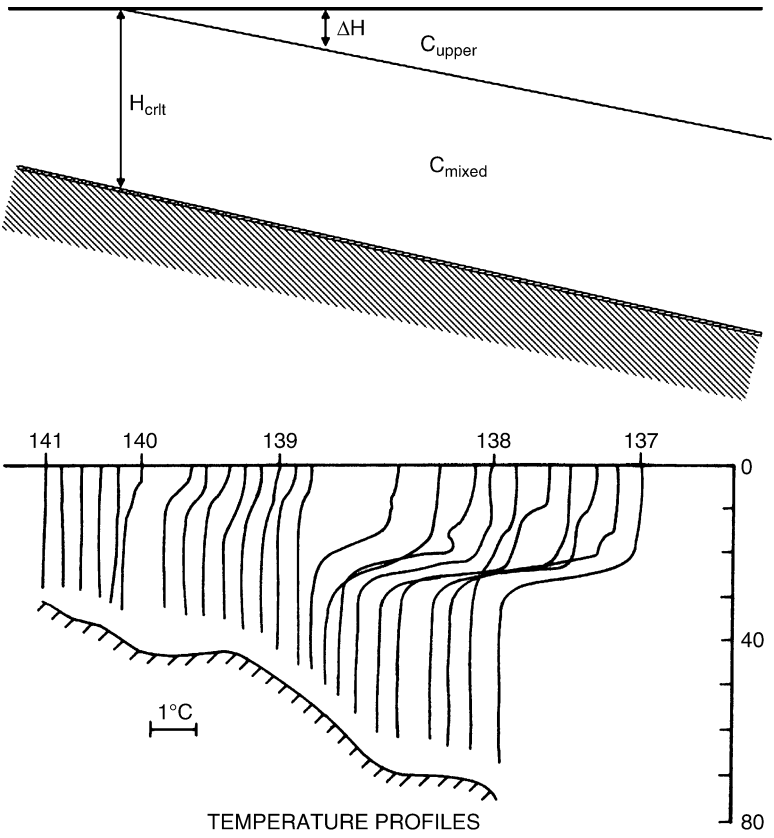


Fig. 2.5 *Top panel* – Simple schematic of a coastal mixing front where the bathymetry is deepening. Past the critical mixing depth, a surface layer forms, resulting in a front. *Lower panel* – Data showing a coastal mixing front from Bowden, referencing Schumacher et al. (1979). Horizontal axis is degrees in longtitude

to warn us that such simple models will often need expansion to cope with the intricacies of the real world.

Shelf break fronts are rather complicated entities, and their genesis, maintenance, structure, and variability are still topics of great interest to the physical oceanographic community. We will make only a brief mention of the genesis and maintenance of these fronts, as these topics are more of interest to physical oceanographers, but will discuss their structure and variability in more detail, as these are of direct acoustic importance.

Historically, the existence of shelf break fronts was explained by *assuming* that there were two horizontally distinct water masses near the shelf break, and that the front and the flow (mostly along the shelf) associated with it were generated and maintained by a mechanism called "geostrophic adjustment," whereby the density gradient force and Coriolis forces balance each other. An alternative to this "almost assuming the answer" type of theory was given by Gawarkiewicz and Chapman

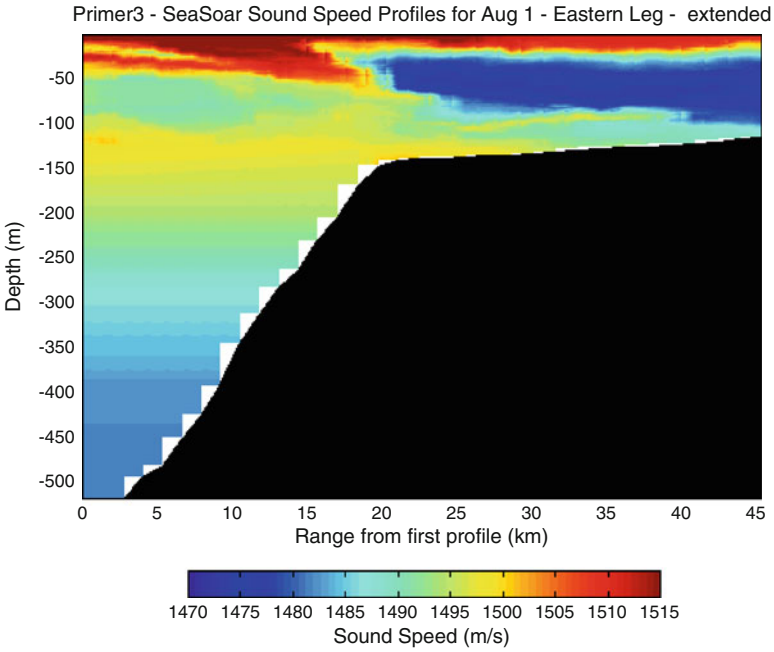


Fig. 2.6 Shelf break front in the Mid-Atlantic Bight measured by SeaSoar undulating CTD as part of the PRIMER experiment in 1996. Warm slope water (to the *left*) meets cold shelf water (to the *right*), creating the front. Much additional structure is seen, in the form of (1) a warm surface mixed layer, (2) a "foot of the front" protrusion of warm, salty water onto the shelf near the bottom, and (3) a 0–50-m depth "downwelling cell" of very warm water just seaward of the shelf break. These additional features all have significant acoustic impact

(1992), who showed that by looking at how the bottom friction affects flows near the shelf break, one could generate and maintain shelf break fronts with absolutely no assumption of horizontally distinct water masses. The Gawarkiewicz/Chapman theory provides a very satisfying explanation of these fronts, but like our mixed layer model above, it is too simple to provide all the acoustically important details that one sees in the real ocean, as, for example, in Fig. 2.6. Larger, data-assimilating "primitive equation" regional oceanographic models can give better pictures of real frontal structure, but as was the case with the mixed layer (discussed above), the amount of input needed to make such models describe a front in adequate detail can be large. Because of this, our predictive capability, even while using large models, must honestly be described as limited at this time.

The dynamics of shelf break fronts are interesting for multidisciplinary acousticians to learn, but the space–time structure of the shelf break front is of far more practical concern. The toy "vertical wall" model that we showed in Fig. 2.2(3) is fine for examining the acoustical physics of fronts in a simple way, but is inadequate in general. In particular, it misses many of the important features of the real front, particularly their across-shelf slope, their along-shelf structure, and

their variability and inherent stability with respect to perturbations. We examine these next. It is observed that coastal fronts, including shelf break fronts, have a bottom-to-top slope on the order of 10^{-2} (Bowden 1983). For shelf break fronts, the bottom or "foot" of the front is at or slightly inshore of the shelf break, with the surface expression being $\sim 10^2 H$ (where H is the water depth at the foot) seaward. This gives us about a 10-km frontal width for $H = 100$ m, a not unreasonable number considering five to ten kilometers is a common result. Going along the front in the along-shelf direction, the first-order assumption based on simple models is that the front is laterally symmetric, i.e., has an infinite correlation length in that direction. But, again, that is a gross oversimplification, and in fact along-shelf correlation length can be as short as the across-shelf length, as it was for the PRIMER experiment front shown in Fig. 2.6. In that experiment, a radially symmetric Gaussian correlation function with scale length ~10 km actually fit the frontal and near-frontal oceanography structure rather well (Sperry et al. 2003). The exact correlation length of shelf break fronts in the along-shelf direction is generally a function of how much the system is perturbed by eddies and other turbulent ocean processes so that it is hard to ascribe a number a priori. Our guess of "between the across-shelf scale length and infinity" is rather unsatisfactory, but it is probably reasonable. As to the stability of these fronts, they are found to reform after being severely perturbed in hours to days, so we can ascribe some real persistence and permanence to them.

Eddies and filaments. Continental shelves, particularly broad western continental shelves, are often located in close proximity to large, strong deep-water current systems. Two spectacular western boundary current examples are the Gulf Stream and the Kuroshio in the Northern Hemisphere, which border the US and Asian shelves, respectively. These currents routinely spawn large eddies and filaments, many of which travel into shallower water (to a distance determined in large part by their vertical extent compared to the shelf bathymetry) and create large sound speed disturbances. Thus, knowing what the onshore eddy and filament radiation field is in a coastal region is important to shallow water acoustics.

For the purposes of acoustics, we would like to have the space, time, and sound-speed perturbation scales of these features. In a somewhat oversimplistic view, the sound-speed perturbation is dictated simply by the differences between the water masses of the eddy/filament and the shelf water. In the Mid-Atlantic Bight (MAB), sound-speed differences of 30–40 m/s between shelf and eddy waters are typical. Obviously, the perturbation magnitude will be highly regionally dependent.

In terms of the (horizontal) spatial scales of the eddies and filaments, one goes from the comparatively large scales of the deep-water features (e.g., ~50 km diameter for Gulf Stream eddies and filaments) to smaller scales on the shelf (5–7 km was typically observed in the MAB). The radius R of these objects is roughly given by the internal deformation radius defined previously, $R = (g'H)^{1/2}/f_C$. In the vertical direction, one can see a large variety of scales, going from a few meters to full water depth. Again, the variability seen is regionally dependent and complicated.

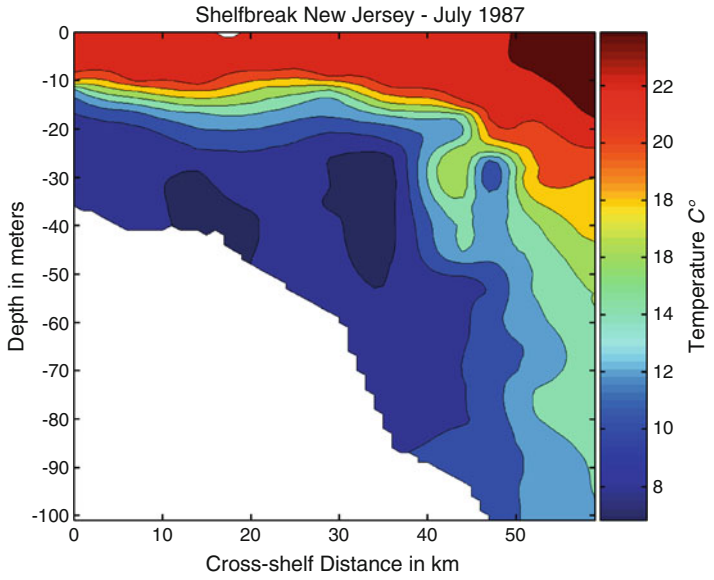


Fig. 2.7 Horizontal acoustic duct created by ocean filamentary feature. Horizontal temperature differences over ~5 km are from 7 to 10°C, or up to 40 m/s in sound speed

In that eddies and filaments are turbulence phenomena, the examination of a turbulence spectrum would seem to be a sensible way to characterize these irregular features. Rather interestingly, looking at the 2D wavenumber spectra of MAB eddies and filaments from satellite, Advanced Very High Resolution Radiometer (AVHRR) thermal imagery has produced k^{-2} spectra, characteristic of sharp-edged features. Vertical wavenumber spectra are harder to obtain, and we know of no readily available estimates of the wavenumber spectrum for shelf eddies and filaments. This is an area that needs further investigation for acoustics purposes, as well as for the other oceanographic disciplines.

We should note that filamentary features can also create acoustic ducts; an example is shown in Fig. 2.7. In this figure, one sees a warm water filament isolating (in the x–z plane) a parcel of cold water, which creates a duct between the warm filament and the warm front. This duct "into the page" way extends for many kilometers and is likely to be curved in the x–y plane as well.

Surface ducts. There are three types of surface ducts one encounters in shallow water that might be of importance to low- and mid-frequency acoustic propagation (1) bubble cloud ducts, (2) pressure gradient ducts, and (3) surface buoyancy plume ducts.

It is well known that a surface bubble layer is created by wave breaking and spilling during wind and storm events, and that this layer has an exponentially decaying profile and a depth on the order of a meter. Farmer and other ocean bubble researchers have made simultaneous measurements of the bubble population and size distribution as a function of depth and time with multifrequency inverted echo

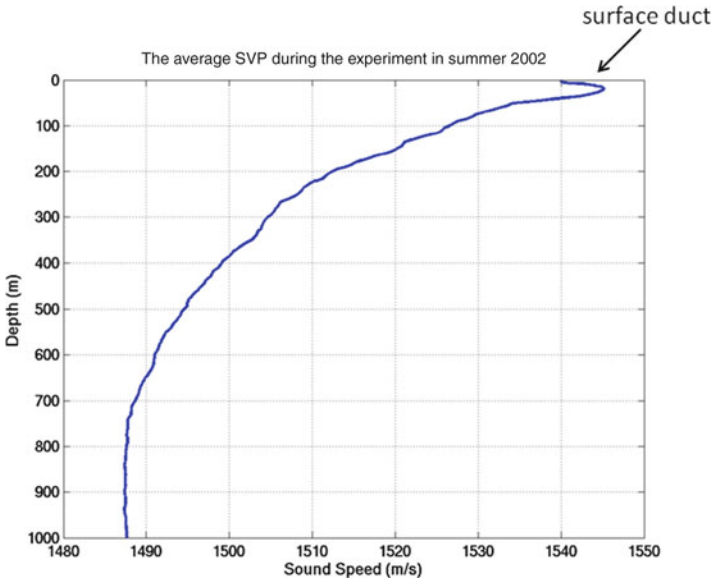


Fig. 2.8 Surface duct created by Mississippi River outflow off the coast of Louisiana. The duct of diluted fresh water is only 5 m/s in strength

sounders, which allow the calculation of the resulting (dispersive) sound-speed anomaly profile. Using the surface ambient noise that is created by such wave events, Farmer and his colleagues were able to show the trapping of some of the ambient sound in the 40 Hz–20 kHz range, with the distinctive modal structure one expects from waveguide propagation (Farmer and Vagle 1989). This is obviously an intermittent and highly variable sound duct, but a real one nonetheless, particularly as frequency increases.

A pressure gradient surface duct can be created when the water column is isothermal and isohaline over the top 10–20 m (typical of a well-mixed surface mixed layer), giving the 0.017 s^{-1} pressure gradient a chance to form a slightly upward refracting surface duct. This duct can channel sound from near-surface sources quite effectively, especially in calmer conditions where surface scattering out of the duct is unlikely to happen. This duct is often called "the surface duct" by mid-frequency sonar operators, as this has the biggest effect in that frequency range. Again, this is an intermittent duct that depends upon a restricted range of conditions for its formation. The range and extent of such a duct are likely to be dictated by the correlation length of the surface mixed layer, a number not easily available.

Buoyant river plumes are a common feature on continental shelves, and are well studied at this point in time. An example of a river plume surface layer signal is shown in Fig. 2.8. It was observed by DeRuiter et al. (2006) that this plume was able to trap seismic airgun signals with frequencies over 300 Hz, the cutoff frequency of this particular duct. Thus, we would not only note these ducts as being viable shallow water features, but would also caution that they are (at present) hard to predict.

Storm surges (*coastally trapped waves*). There is perhaps one more rather large-scale ocean feature that bears discussion here, i.e., storm surges, which can raise the sea level several meters. It is well known that storms push water away from them, and that the water pushed by the storm can precede the storm in arrival. This is due to the storm surge being describable by a Kelvin wave, a coastally trapped wave that has wave speeds given by $c = (gH)^{1/2}$, which gives $c = 25$–45 m/s in waters 60–200 m deep. Since storms typically travel at 10–15 m/s, the surge usually outstrips the storm and is seen first. The coastally trapped Kelvin wave also has the highest amplitude at the shore and decays away in amplitude exponentially with distance from the shore. Thus one sees the large, and often perilous, surges near the shore (several meters), but less of an effect further out (1–2 m). The state of the art in forecasting storm surges is actually rather good at this point, as they have a pronounced human impact. Thus, for the purposes of shallow water acoustics, we can take this as a known and understood process.

2.4 Dynamics of the Ocean Surface: Surface Waves

Surface waves are perhaps the most familiar phenomena from physical oceanography and also of great importance to shallow water acoustics, since they introduce a range-dependent water depth and waveguide boundary condition. Again, a vast literature on the topic exists, and we must constrain our treatment here to the "useful nuggets" for SW acoustics. A short section on the basic theory of surface waves is presented in Appendix A; here, we will only consider shallow water applications of surface waves.

Let us first look at the case of 1D surface waves to illustrate some simple concepts before moving to the more realistic case. Considering only waves traveling in the x direction, the elevation of the sea surface $\zeta(x,t)$ may be written in a discrete sum form as

$$\zeta(x,t) = \sum_{n=1}^{\infty} a_n \exp[i(\tilde{q}_n x - \Omega_n t + \varphi_n)], \tag{2.17}$$

where a_n is the amplitude of the nth component of the wave spectrum which has wave number $\tilde{q}_n$, frequency Ω_n, and a random phase φ_n which ranges from 0 to 2π uniformly. The dispersion relation relating the frequency and wavenumber is [see (A.35)]:

$$\Omega^2 = g\tilde{q} \tanh \tilde{q}H, \tag{2.18}$$

where g is acceleration of gravity and H is depth. We should note that for coastal waters, where the depths we consider are 10–200 m, the dispersion relation most generally falls between the long wave (shallow water) and short wave (deep water)

limits, and that one is generally well advised to use the full dispersion relation in (2.18), rather than one of the limiting cases. However, the deep-water dispersion relation $\Omega^2 = g\tilde{q}$ is reasonable for many shallow water cases; so if one needs to approximate, this is probably the better form.

If we now extend the wavenumber spectrum to two dimensions, i.e., the x–y plane [see (A.62)–(A.66)], we can define a wavenumber–frequency spectrum, $G(\tilde{\vec{q}}, \Omega)$, where $\tilde{\vec{q}} = (\tilde{q}\cos\alpha, \tilde{q}\sin\alpha)$ is the magnitude of the 2D wavenumber vector, and α is the azimuthal direction. The most usual measurement of waves is the "polar" spectrum containing both frequency and direction information, which we can relate to the wavenumber–frequency spectrum by

$$G(\Omega, \alpha) = 2\int_0^\infty G(\tilde{\vec{q}}, \Omega)\tilde{q}d\tilde{q}. \tag{2.19}$$

This quantity is the one that is measured by standard instruments and is of most use to acoustics. For this spectrum, the variance of the sea surface height is determined as

$$\sigma^2 = \int_0^{2\pi}\int_0^\infty G(\Omega, \alpha)d\Omega d\alpha. \tag{2.20}$$

An often-quoted measure of wave displacement, the significant wave height H_s, which tells one what the average height of the biggest 1/3 of the waves is, is related to this by

$$H_s = 4(\sigma^2)^{1/2}.$$

Often wave buoys do not have tilt sensors in them and just measure the frequency content of the surface waves via accelerometers. In this case, one has effectively integrated the frequency-directional spectrum over angle, giving

$$G(\Omega) = \int_0^{2\pi} G(\Omega, \alpha)d\alpha. \tag{2.21}$$

Having defined formally what the wave spectra are, it is also useful to describe some "popular parameterizations" of these quantities, as these are often employed in calculations. This is generally done by multiplying a wave-directional spectrum by a wave frequency spectrum. Two popular parameterizations of the wave frequency spectrum are the Pierson–Neuman and the Pierson–Moscovitz spectra. The Pierson–Neuman spectrum is

$$G_{PN}(\Omega) = C\Omega^{-6}\exp\left[-2\left(\frac{g}{\Omega v}\right)^2\right], \tag{2.22}$$

where $C = 2.4\,\mathrm{m}^2/\mathrm{s}^5$, and v is the wind speed in m/s. The more recent Pierson–Moscovitz spectrum is given by

$$G_{\mathrm{PM}}(\Omega) = 8.1(10^{-3})g^2\Omega^{-5}\exp[-0.74(g/\Omega v)^4]. \tag{2.23}$$

The directional spectrum, denoted as $G(\tilde{q},\alpha)$, is often given by a cosine-to-a-power form, i.e.,

$$G(\tilde{q},\alpha) = \begin{cases} b\cos^{v(\tilde{q})}\alpha, & |\alpha| \le \pi/2 \\ 0, & |\alpha| > \pi/2 \end{cases}. \tag{2.24}$$

In (2.24), $v(q)$ varies from 10 at low frequencies to 2 at the higher frequencies. The factor b is determined by the following normalization condition:

$$\int_{-\pi}^{\pi} G(\tilde{q},\alpha)\mathrm{d}\alpha = 1. \tag{2.25}$$

In addition to the cosine form, a sech^2 form has also been used for coastal spectra, and we refer the reader to Donelan et al. (1985) if this form is of interest.

As a last note about surface wave spectra in shallow water, the distance from the measurement site to the shore, called the fetch, often needs to be considered. A good account of the evolution of coastal wave spectra (including fetch and other coastal effects) can be found in Hasselmann et al. (1980), which describes the results of the Joint North Sea Wave Project (JONSWAP).

2.5 Dynamical Processes Inside the Ocean: Tides and Internal Waves

Tides. There are two types of tides of interest to shallow water acoustics: barotropic and baroclinic. A barotropic tide affects the entire water column uniformly, whereas a baroclinic tide produces a nonuniform vertical structure. The barotropic tides are the most familiar to us and so we will address them first.

The barotropic tide produces three effects of interest to shallow water acoustics (1) a periodic increase and decrease of the water depth, (2) a current field, and (3) an advection of ocean structure along the tidal ellipse. The amplitude and phase of the tidal signal (both in water depth variation and current) are a strong function of where one is geographically, as the local coastline and bathymetry are major factors in the tidal equations. Thus, we cannot provide any more useful guidance to the reader than to consult local tidal tables when doing an experiment. Moreover, these tables will probably be far more accurate in describing water depth variation than the current, as tide gauges are common along coastlines, whereas current measurements are sparse. (However, this is fortuitous, in that current is a

second-order determinant of sound speed.) As to the periodicity of the tidal signal, that too is locally variable, though there are two major tidal components that dominate – semidiurnal (12.4 h) and diurnal (25 h). One most often sees the semidiurnal tide, though in many locations the diurnal tide or mixed diurnal–semidiurnal tides are observed. Again, this is locally variable and the rule is to look at local tide charts. Since the barotropic tide is a well-known and long investigated phenomenon, we will simply refer the reader to some of the standard introductory texts for more detail. Specifically, the texts by Pond and Pickard (1983) and Bowden (1983) provide a good starting point. We now turn to the acoustic effects of barotropic tides.

The first tidal effect, the water depth variation, is often of importance acoustically even though it would seem that the ~1-m variation typical of coastal regions should be negligible. But an ~1% perturbation of the water column depth can perturb modal eigenvalues and travel times just as much as a significant perturbation in either the bottom or the water column sound speeds, and so must be taken carefully into account when using modal inverse methods for obtaining medium properties. In general, one must look to how the acoustic quantity used scales with water depth to see how the tidal signal affects a particular application. Turning to the currents, there is again a wide local variability, but an average value of ~0.5 m/s (or 1 knot) would not be far off the mark for coastal waters. As this is a fraction of a percent of the water column sound speed (~1,500 m/s), the current usually does not need to be considered when looking at the sound speed profile of a particular shallow water region. Current-related source-speed effects, however, can be considerable in that speeds of fish, marine mammals, ships, AUVs, etc., are of the order 1–10 m/s, which makes the tidal current a 5–50% effect in reference frames where it can be noticed. Finally, we mention the horizontal advection of ocean structure by tidal currents, particularly the temperature structure to which acoustics is most sensitive. If we take ocean structures such as eddies, fronts, and internal waves to be frozen in shape, the tides will move these features around their tidal ellipses. The largest excursions are represented by the time integral of the tidal velocity components (along-shelf and across-shelf being the generally preferred directions) over a half period, as the tide then reverses direction. These excursions are of the order of 1–10 km, which is significant, as the coastal ocean commonly has significant horizontal sound-speed structure gradients over these scales.

We next turn to the baroclinic tides, or the so-called internal tides in shallow water. Our dealings with the baroclinic tide will be brief in this section, simply because the internal tide is an internal wave of tidal frequency, and so is most appropriately included in our discussion of internal waves. However, a few points should still be made here, on both the oceanography and the acoustics, before we pass to the internal wave section. First, the linear coastal internal tide often looks like a long wavelength (10–40 km), two-layer system (less dense water above more dense water) sinusoidal wave propagating at a speed of (as a rough average) 0.25–0.5 m/s from the shelf break toward the shore, with an amplitude of 5–10 m. Second, the internal tides can have “critical latitudes” beyond which they cannot exist as propagating disturbances, i.e., they become evanescent,

decaying waves. Third, the baroclinic tides are far more variable than the barotropic tides (due to their dependence of their propagation properties on the complex thermohaline and current structure of the ocean through which they move) and so are far less predictable. One does not find internal tide atlases, though there is now a fairly extensive literature on such tides, and indeed an atlas for nonlinear internal tides recently appeared (Jackson and Apel 2002; Jackson 2004).

Acoustically, linear internal tides tend to create a slowly evolving range dependence of the acoustic waveguide, and so can generally be accounted for using adiabatic normal mode theory. However, the nonlinear internal tides create sharp horizontal gradients in the ocean structure, producing acoustic effects which are much more substantial and interesting.

Internal waves. Elements of the general theory of internal waves in a stratified liquid are considered in Appendix A. In this chapter, we will consider properties of the internal waves on the oceanic shelf and their connection with the acoustic properties of a shallow water waveguide. To begin, let us revisit the properties of the seawater taking into account its compressibility.

We begin with an equilibrium density depth distribution $\rho = \rho_0(z)$, formed by taking into account the compressibility of water. We then consider the adiabatic displacement of a selected volume dV (the mass of this volume is $dm = \rho_0(z)dV$) by depth dz. Its density at the depth $z + dz$ is changed by $d\rho = \beta_a \rho_0^2(z) g dz$ [see (2.2)]. Using the connection between the compressibility and the sound speed, we can write the resulting density variation of the displaced volume as

$$\delta\rho = \left(\frac{\partial\rho_0}{\partial z} - \frac{\rho_0 g}{c^2}\right)\delta z \tag{2.26}$$

which contains a part (the second term on the right side) formed by hydrostatic pressure.

The "Archimedes force" dF_A (i.e., the buoyancy, or restoring force) exerted on this volume has the value

$$dF_\mathrm{A} = \rho_0 dV\left(\frac{g}{\rho_0}\frac{d\rho_0}{dz} - \frac{g^2}{c^2}\right)dz. \tag{2.27}$$

So for the frequency of harmonic oscillations [the Vaisala frequency, introduced in (A.104)], we have the expression

$$\tilde{N}^2(z) = \frac{g}{\rho_0}\frac{d\rho_0}{dz} - \frac{g^2}{c^2}. \tag{2.28}$$

We now introduce the so-called potential density $\rho_\mathrm{p}(z)$ by the equation

$$\frac{\partial\rho_\mathrm{p}}{\partial z} = \frac{\partial\rho_0}{\partial z} - \frac{\rho_0 g}{c^2}. \tag{2.29}$$

If water is taken to be incompressible or gravitation is ignored, then the real density and potential density are the same. In other words, the potential density can be formed by the compressible density if we throw out gravitation. The difference between the real density and the potential density is called the adiabatic density. The stability of the water column is determined by the potential density, as well as the oscillations in the vertical plane and the Vaisala frequency. In a similar way, we can also introduce the potential and adiabatic distributions for the temperature and salinity depth dependence.

The second term on the right side of (2.28) is of the order ~4×10^{-5} s^{-2}, whereas the first term can be ~10^{-3}–10^{-4} s^{-2}. Thus, for shallow water (or more exactly for upper ocean layers – several hundred meters), we can neglect the second term in the Vaisala frequency and thus use (A.94). We will use (A.94) in our following discussions of internal waves.

Let us now consider some numerical estimates. In shallow water, we can typically have temperature jumps of several degrees (3–5°C) over a depth interval of 10–20 m. This means that the temperature gradient can be 0.1–0.5°C/m. From this, it is possible to estimate the relative density gradient and then the Vaisala frequency $\tilde{N} \approx \sqrt{\frac{g}{\rho_0}\frac{d\rho_0}{dz}} = \sqrt{g\beta_T \frac{dT^\circ}{dz}} \leq 10.$ cph.

Using the aforementioned connections between the thermodynamic parameters of seawater, (2.2)–(2.6), we can establish the relation between internal waves and the fluctuations of the sound-speed profile, an important relation for underwater acoustics.

We begin with some equilibrium distribution of the water layer parameters: $\rho_0(z)$, $T^\circ(z)$, $c(z)$. If we have a displacement of a selected water volume by δz, then the corresponding fluctuation of the water density at a given depth (neglecting small corrections due to compressibility) is $\delta\rho = \frac{d\rho_0}{dz}\delta z$; correspondingly, the sound speed will be changed by $\delta c = \frac{\partial c}{\partial z}\delta z$.

As mentioned, density and temperature fluctuations are connected by $\delta\rho = \frac{\partial\rho_0}{\partial T^\circ}\delta T^\circ = \rho_0\beta_T\delta T^\circ$. For seawater, we have that $\beta_T \sim 1.3 \times 10^{-4}\,(^\circ\mathrm{C})^{-1}$. If we use these, i.e., the coefficient of thermal expansion and the variability of the sound speed with temperature, then we obtain

$$\frac{\delta c}{c} = \frac{1}{c}\frac{\partial c}{\partial T^\circ}\delta T^\circ = \frac{1}{c}\frac{\partial c}{\partial T^\circ}\frac{1}{\rho_0\beta_T}\delta\rho = \frac{1}{c}\frac{\partial c}{\partial T^\circ}\frac{1}{\rho_0\beta_T}\frac{\partial\rho}{\partial z}\delta z = \frac{1}{gc}\frac{\partial c}{\partial T^\circ}\frac{1}{\beta_T}\tilde{N}^2(z)\delta z.$$

If we denote

$$\tilde{Q} = \frac{1}{gc}\frac{\partial c}{\partial T^\circ}\frac{1}{\beta_T} \tag{2.30}$$

then

$$\delta c = \tilde{Q}c\tilde{N}^2(z)\delta z. \tag{2.31}$$

Using the range of values we considered, we can estimate numerically that $\tilde{Q} \approx 2.4\,\mathrm{s}^2/\mathrm{m}$. In the monograph edited by Flatte (1979), it is shown that this constant does not vary significantly with temperature and depth.

Varieties of internal waves. Due to the rotation of the Earth, the so-called inertial waves of frequency $\Omega_i = 2\Omega_\mathrm{E} \sin\theta$ exist, where $\Omega_\mathrm{E} \sim 0.04$ cph is the rotation frequency of the earth and θ is the latitude. These inertial waves define the lowest propagating wave frequency in the IW band, whereas the biggest Vaisala frequency defines the top of the propagating IW band. The inertial frequency varies from two cycles per day at the poles to zero cycles per day at the equator, whereas the maximum buoyancy frequency is usually on the order of 10–20 cph. This means that in the equation determining the internal waves, (A.108), $\Omega_i \ll N$ in the denominator. However, we cannot simply throw this term out, because (as will be seen in the following discussion) inertial oscillations often appear strongly in the IW spectrum, providing they are obtained via long-time observations (several days or more). Thus, we can neglect inertial waves for most experiments with durations on the order of several hours, but we should take inertial waves into account for experiments on the order of 50–100 h or more. We would also note that inertial oscillations are due to water being accelerated, with the dominant mechanism being sudden wind events. Additionally, the particle paths for inertial waves are horizontal so that their effect on acoustics is actually minimal.

Two flavors of propagating IWs are found in stratified coastal waters: linear and nonlinear waves. The linear waves, found virtually everywhere, obey a standard linear wave equation for the displacement of the surfaces of constant density (isopycnal surfaces). The nonlinear IWs are generated under somewhat more specialized circumstances than the linear waves and obey a wide variety of wave equations (Apel et al. 1995). The simplest description is the familiar Korteweg-deVries equation (KdV), which governs the horizontal components of the nonlinear internal waves. Both types of internal waves can be illustrated by a simple two-layer model (see Appendix A), i.e., the three-layer model with the thermocline shrunk to zero extent. Using the two-layer model, we can look at some typical wave parameters. For a more or less common situation, where $H_1 = H_2$ and $\Delta\rho/\rho = 2.0 \times 10^{-3}$, one obtains that ratio of speeds of internal and surface waves is $\tilde{c}_\mathrm{int}/\tilde{c}_\mathrm{surface} = 1/45$; typical wave speeds would be $\tilde{c}_\mathrm{int} = 0.8\,\mathrm{m/s}$ and $\tilde{c}_\mathrm{surface} = 36\,\mathrm{m/s}$. However, while the small density contrast between ocean layers makes the internal wave speed small, it also contributes to making internal wave amplitudes large compared to surface waves. Typically, internal wave amplitudes are of order 5–10 m in coastal regions; however, some coastal nonlinear internal waves can have amplitudes of 100 m or more! Also, the dispersion relations for surface and internal waves show that the internal waves will generally have much longer wavelengths than surface waves. The highest frequency linear internal waves have $\lambda \approx 100\,\mathrm{m}$, whereas the low-frequency "internal tides" have wavelengths on the order of tens of kilometers. By comparison, surface wave wavelengths are tens to hundreds of meters.

Linear internal waves. We next look at the spectrum of the linear internal waves in shallow water, following Colosi et al. (2001). In doing this, we will look at a continuously stratified medium, as opposed to the two-layer simplification. Currently, a popular approach is to use a wavenumber spectrum much like the well-known Garrett and Munk (1975) spectral description appropriate for deep water (Yang and Yoo 1999). A prime descriptor of the IW is the amplitude of the displacement of a water layer of constant density, as a function of the coordinate in the horizontal plane and time, $\zeta_{\mathrm{IW}}(\vec{r}, t)$ (see Appendix A). We consider the internal wave field to be a linear superposition of waves of the form,

$$\zeta_{\mathrm{IW}}(\vec{r}, t) = \int_{-\infty}^{\infty} \int_{-\infty}^{\infty} d\tilde{q}_x d\tilde{q}_y \sum_{l=1}^{\infty} S_l(\vec{\tilde{q}}) \Phi_l(z; \tilde{q}) \exp\left[i \left(\vec{\tilde{q}} \vec{r} - \Omega_l(\tilde{q}) t \right) \right], \tag{2.32}$$

where $\Omega_l(\tilde{q})$ is the internal wave dispersion relation, $\Phi_l(z; \widetilde{q})$ are the internal wave eigenmodes, and $S_l(\vec{\tilde{q}}) = S_l(\widetilde{q}_x, \widetilde{q}_y)$ are the amplitude distribution of the internal waves, taken to be complex zero mean Gaussian random variables with cross spectral density

$$\left\langle S_l(\vec{\tilde{q}}) S_m(\vec{\tilde{q}}') \right\rangle = G_l^{\mathrm{s}}(\vec{\tilde{q}}) \delta_{lm} \delta(\vec{\tilde{q}} - \vec{\tilde{q}}'). \tag{2.33}$$

The quantity $G_l^{\mathrm{s}}(\vec{\tilde{q}})$ is the spectral density of the random field of internal waves. We consider this value to be the main characteristic of the random IW field. In the following discussion, it will be called the "spectrum" of the IW. The modes $\Phi_l(z; \widetilde{q})$ in (2.32) are obtained by solving the linear internal wave equations (A.108)–(A.110) with the appropriate input for $N(\widetilde{z})$.

We note that there are several variants of the mode (A.108) extant in the literature, depending on exactly what physics are included in the modes. One commonly sees (A.108) without the Coriolis parameter in the denominator, which ignores the effects of the Earth's rotation (as we discussed). One can also add the important effect of vertical current shear to (A.108), which results in the so-called Taylor–Goldstein equation. Equation (A.108) is easily solved with standard finite difference techniques. It should be noted that shallow water has a very "red" IW modal spectrum. Because of this, one generally needs to look at only the lowest few modes, often just the first.

The function $G_l^{\mathrm{s}}(\vec{\tilde{q}})$ is called the spectrum of the internal waves, and has the physical meaning of the energy density of the internal waves in a given gravitational mode for a given wave vector in the horizontal plane. It is one of the most important characteristics of the internal wave field. In deep water, this spectrum has been best described by the work of Garrett and Munk (1975). In shallow water, there have been many different attempts to extend this spectrum. However, it does not appear possible to find a common spectrum appropriate for all shallow water areas, where there are significant sources and sinks, directional waves, etc. But one still needs something to work with in SW, and so we describe one of these efforts as an example.

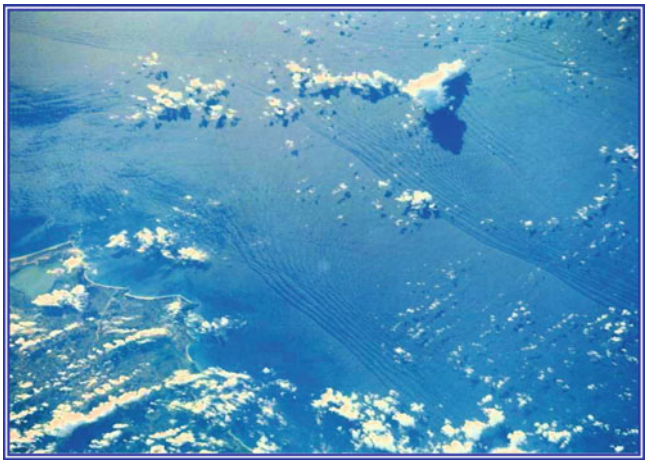


Fig. 2.9 An observation showing the parameters of internal solitary waves as presented in the work by Xiaofeng Li et al. (2000)

As mentioned, Yang and Yoo (1999) have shown that a useful model, which fits the comparatively sparse existing data on shallow water linear internal waves, looks like the GM spectrum, with

$$G_j^{\mathrm{S}}(\tilde{q}_x, \tilde{q}_y) = \varsigma_0^2 \frac{\tilde{N}_0}{\tilde{N}(z)} \frac{M_l}{(j^2 + j_*^2)^q} M_{\tilde{q}} \frac{\tilde{q}_j^{p-2} (\tilde{q}_x^2 + \tilde{q}_y^2)^{1/2}}{(\tilde{q}_x^2 + \tilde{q}_y^2 + \tilde{\sigma}_z^2)^{\frac{p+1}{2}}}, \tag{2.34}$$

$$\tilde{q}_j = \frac{\pi f j}{\tilde{N}_{0B}} \quad \tilde{N}_{0B} = \int_0^H N(z) dz, \tag{2.35}$$

where H is depth of the waveguide, $j^* \sim 1$, $q \sim 1$, $p \sim 2.7$, f_{C} is the Coriolis parameter, and M_j, $M_{\tilde{q}}$ are normalizations to provide a depth-dependent displacement variance of $\varsigma_0^2 \tilde{N}_0 / \tilde{N}$. We note that for the GM model, one has $j^* \sim 3$, $q \sim 1$, $p \sim 3$, $\zeta_0 \sim 7.3$ m, and $\tilde{N}_0 \sim 3$ cph. Also, note that (2.34) is a homogeneous, isotropic spectrum, which only depends on the magnitude of the horizontal wavenumber. An efficient scheme for the numerical evaluation of such spectra was provided by Colosi and Brown (1998) and could be adapted for shallow water environments of variable water depth and stratification.

In closing this section, we will note that an isotropic directional spectrum may not be a good assumption for the linear wave field that is found at the tail of a nonlinear internal wave train. This will be discussed later in the book.

Nonlinear internal waves. As mentioned many times, nonlinear internal waves are also common on continental shelves. Observations of coastal nonlinear internal waves are commonly shown, and we present two typical ones below, in Figs. 2.9 and 2.10 (airborne photos).

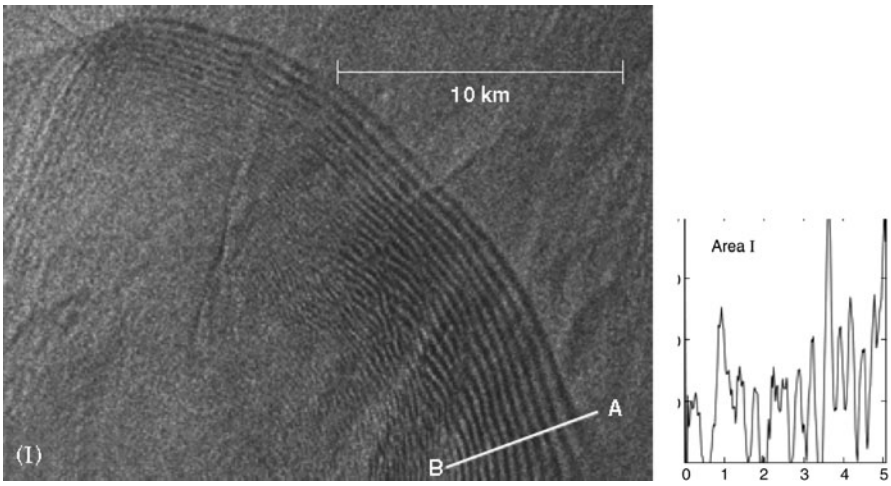


Fig. 2.10 Solitary waves often exist in the form of packets (or trains) propagating toward the coast line. An illustration of one of these trains on the NJ shelf is presented above

Table 2.2 Results of observations of coastal nonlinear internal waves

			Average wavelength per packet (m)		Number of wave crests				
N	Number of packets	Length (km)	1	2	1	2	Group velocity (m/s)	Tide period (min)	Water depth (m)
I	1	–	410	–	11	–	–	12:40	100
II	2	11.2	560	580	6	11	0.25	12:40	50
III	2	13.8	560	780	7	9	0.30	12:40	35
IV	2	9.5	630	760	9	7	0.21	12:40	35

The results of processing observations such as the one above in Fig. 2.10 are presented in Table 2.2, showing typical values of coastal internal solitary wave trains. We would note that these values, while "typical," also vary with location, times, and season.

One finds a vast literature available on this topic of nonlinear internal waves, indeed far larger than that concerning linear internal waves (which are oft-times harder to observe in shallow water!). The reader interested in more detail is referred to the review article by Apel et al. (1995) and the ONR workshop report authored by Duda and Farmer (1999) for initial treatments and a source of references.

For nonlinear internal waves, function $\zeta(\vec{r}, z, t)$ cannot be presented as a product of the vertical mode on the plane wave, similar to (2.32). Dependence on horizontal coordinates is determined by the nonlinear equation. Let us consider a function of displacement for a fixed depth, for example, $z_{\max}$, where function $\Phi_l(z)$ has a maximum. So we have a function of the horizontal coordinates

$$\zeta(\vec{r},t) = \zeta(\vec{r}, z_{\max}, t). \tag{2.36}$$

This function satisfies a nonlinear equation, depending on our model of the water layers. Many different equations and their solutions are given in the literature (Apel et al. 1995). For our purposes, we will just concentrate on one of the simplest yet most useful nonlinear internal wave equation for shallow water, the KdV equation, which depends only on one spatial coordinate: $\zeta(x,t)$. In the limits of small nonlinearity, weak dispersion, and long waves, one can derive expressions for the displacement of the isopycnal surfaces from their equilibrium levels due to internal waves. In Appendix A, a nonlinear KdV equation is obtained for a simple two-layered liquid. For arbitrary stratification, a similar equation can be used:

$$\frac{\partial\zeta}{\partial t} + \tilde{c}^{\text{ph}}\frac{\partial\zeta}{\partial x} + \alpha\zeta\frac{\partial\zeta}{\partial x} + \beta\frac{\partial^3\zeta}{\partial x^3} = 0 \tag{2.37}$$

where the parameters α, β can be expressed through the waveguide characteristics

$$\alpha = \frac{3\tilde{c}^{\text{ph}}}{2Q}\left\langle\left(\frac{d\Phi}{dz}\right)^3\right\rangle, \quad \beta = \frac{\tilde{c}^{\text{ph}}}{2Q}\langle\Phi^2\rangle, \quad \text{and} \quad Q = \left\langle\left(\frac{d\Phi}{dz}\right)^2\right\rangle. \tag{2.38}$$

In (2.38), Φ is the vertical mode function defined in (A.107)–(A.110), and $\tilde{c}^{\text{ph}}$ is the linear wave phase speed. Equation (2.39) has a very well-known solitary wave (single soliton) solution, which is

$$\zeta(\vec{r},z,t) = \zeta_0 \sec^2\left(\frac{x-\tilde{c}t}{\Lambda}\right). \tag{2.39}$$

In (2.39), ζ_0 is the amplitude, $\tilde{c}$ is the nonlinear wave velocity, and Δ is the characteristic width of the soliton. These are related to the linear speed and displacement via the relations

$$\tilde{c} = \tilde{c}^{\text{ph}} + \frac{\alpha\zeta_0}{3} \quad \text{and} \quad \Lambda^2 = \frac{12\beta}{\alpha\zeta_0}. \tag{2.40}$$

The single soliton solution is a very useful one for acoustics calculations, in that it can be implemented simply. One can also make *ad hoc* trains of solitons by stringing these individual solitons together spatially. The effects of these *ad hoc* soliton train solutions on acoustics are often quite close to that of more elegant oceanographic models, giving them a decided appeal for simple calculational studies.

For the continuously stratified medium case, we can numerically solve the KdV equation to get a time and space evolving train of solitons. The solution methods are standard and give results such as the one shown in Fig. 2.11.

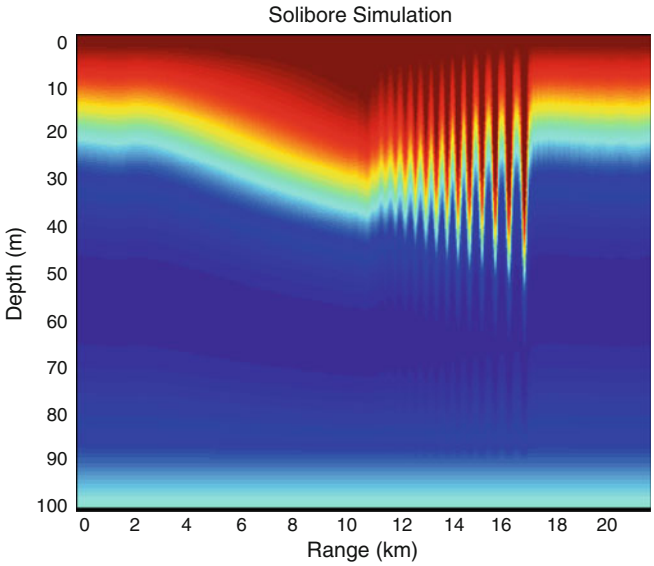


Fig. 2.11 Simulation of a train of solitons using the KdV equation. "Solibore" is a phrase coined to denote the fact that the train of solitons generated has both sharp solitons and a bore-like depression of the main thermocline

In concluding the discussion of internal waves, we will merely restate that the solutions shown above are some of the simplest ones available and as such should be useful for first-order acoustic calculations. However, there are many more complications and nuances of the internal wave field, and we would caution the reader that these simple solutions do not fully capture the real wave field. For this, one may have to pursue more detailed alternatives.

2.6 Experimental Studies of Coastal Internal Waves

We have so far considered the general properties of internal waves in a shallow water region. Next, we will illustrate our analysis by examples of detailed observations of the internal wave field in two shelf areas (the New York (NY) Bight and Kamchatka). Of the most practical use, we will show how it is possible to construct a model of the sound-speed field in a SW waveguide based on measured data; more exactly, we will see how we can get the spatial distribution of the sound speed using temporal data obtained at a fixed point (or several fixed points). In modeling the IW field for shallow water acoustics, it is best to use robust characteristics of the IW field, as measured in an experiment for a given region. There are generally two easy and robust measurements one can make: temperature

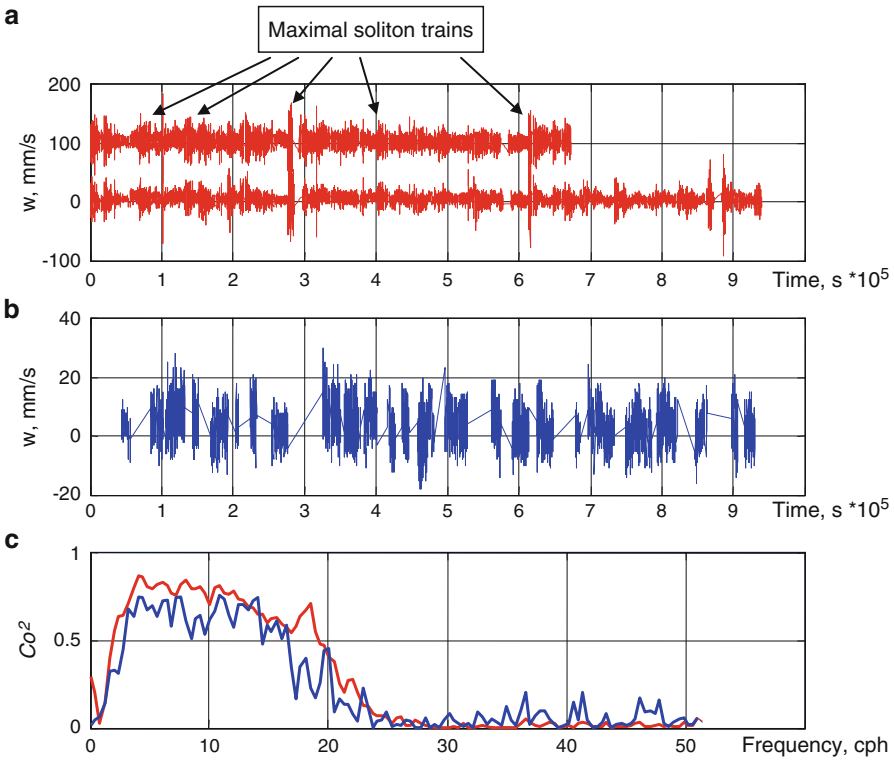


Fig. 2.12 (**a**) Portions of the vertical current velocity records for depth 17 m (*upper line*) and 28.7 m (*bottom line*), (**b**) – record of the "background" segments for depth 28.7 m, (**c**) – coherence function squared (Co^2) between records including soliton trains (*red line*), and between the same records in the background segments (*blue line*)

(simple, cheap thermistor devices abound) and current (e.g., using ADCPs to get vertical profiles of three-component currents is now common). We will look first at current measurements, and then go to temperature.

In discussing the NY Bight, we will examine current measurements of internal waves using some older current velocity meters (the so-called three-axis propeller type). These devices are generally placed at a few vertical points and give values of the three components of velocity $\vec{v}(\vec{u}, w)$ as a function of time. For our work, the vertical component $(w = \partial\zeta/\partial t)$ is obviously the most important one to consider. In Fig. 2.12, we show typical records of the vertical current velocity $w(\vec{r}, z, t)$ including the IW field. These two records were measured simultaneously in the Middle Atlantic Bight (MAB) (Kuzkin et al. 2006). The two current meters were placed at the same location but at different depths, $z_1 = 17$ and $z_2 = 28.7$ m, respectively. The water depth was $\approx$70 m. As may be seen from Fig. 2.12, soliton trains (the pieces with significant amplitude) compose a notable portion of the records.

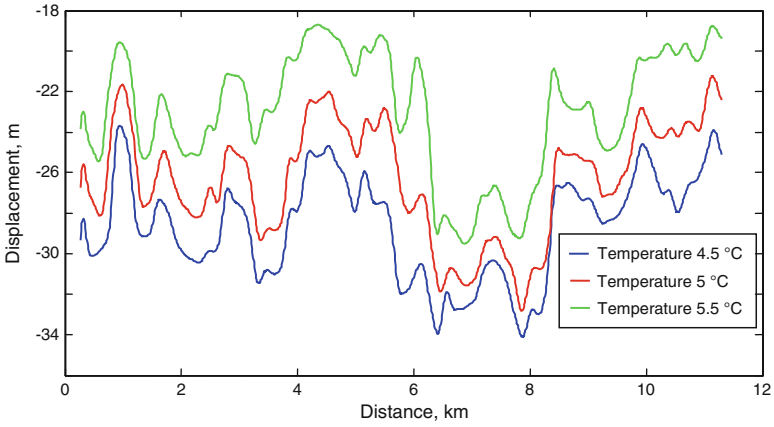


Fig. 2.13 Vertical displacements of isothermal surfaces off Kamchatka

To analyze these results, we will consider the soliton trains and the background waves as independent wave fields in a first approximation. We will also assume that the soliton train is a deterministic process and that the linear background IW field is a random field. Of course, there is significant variability in the nonlinear wave field from tidal period to tidal period (Colosi et al. 2001). However, over one tidal period, one can take the soliton train as a deterministic process for our current purposes. Based on this assumption, we separate the experimental record into background waves and soliton trains. Notice that there is some degree of subjectivity in the choice of the threshold for the separation of background and solitary waves. In order to define this threshold for our case, we can estimate the phase velocity of linear internal waves for our region. Using a simple two-layered model (A.123) and taking the appropriate parameters (depth $H \sim 70$ m, depth of thermocline $H_1 \sim 15$ m, etc.), we get $\tilde{c}^{\mathrm{ph}} \sim 35$ cm/s. We then take the threshold for the amplitude of the vertical current velocity to be less by one order of magnitude or 3.5 cm/s for frequencies less than 10 cph. (This corresponds to an amplitude of the vertical displacements of ~2 m.) For greater amplitudes, we assume that we have deterministic soliton trains, whereas for smaller amplitudes we suppose that we are dealing with a random realization of the background IWs. Results of this separation are shown in Fig. 2.12 for the vertical current velocity records. The coherence ratio[1] for the records with soliton trains and without trains is plotted in Fig. 2.12 as well. We see that a high coherence ratio is found in both cases. This is because the first gravity mode almost invariably dominates the IW field, both for the solitons and for the linear waves.

We can produce additional arguments in favor of this statement. In Fig. 2.13, we show results of measurements of the vertical displacement $\zeta(r, z, t)|_{z,t=\mathrm{const}}$ mode at

[1] Notice that coherence function of two random processes $w_1 = w(x, y, z_1, t)$ and $w_2 = w(x, y, z_2, t)$ for given values $x,\ y,\ z_1,\ z_2$ is defined in the Appendix.

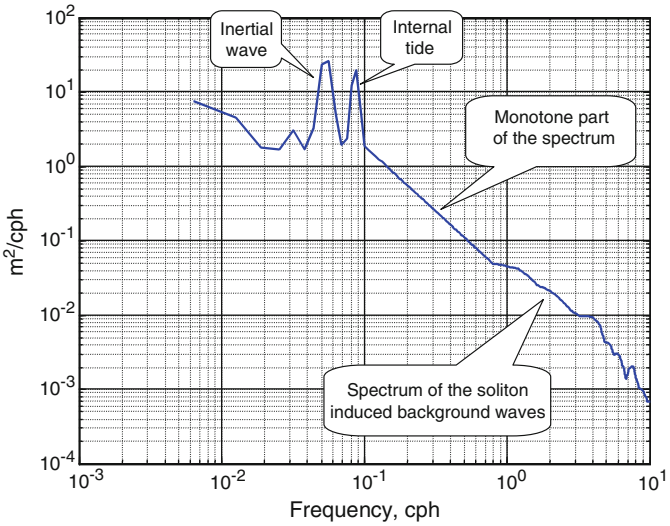


Fig. 2.14 The temporal spectrum of the background linear internal wave field

different depths near Kamchatka. The measurement was carried out using a towed vertical thermistor string. As seen from the figure, the isothermal surfaces oscillate synchronously at different depths. This can take place only if the field is dominated by the first mode.

After the separation of background and solitary waves, we have the samples of the vertical displacements caused by the soliton trains which now can be used to study the effect of intense nonlinear IWs on sound propagation in shallow water. Further details on this topic are given in Chap. 5 of this book. On the other hand, we also have a realization $\zeta(\vec{r}, z, t)$ of the random field. We consider the value $\zeta(x, y, z, t)$ as a random field at the fixed point $\vec{r}, z$ and homogeneous in the horizontal plane so that the power spectrum does not depend on (x, y). We denote it as $G^{\mathrm{t}}(z, \Omega)$; for the background IW, it is shown in Fig. 2.14.

This (averaged and smoothed) spectrum has some important features. First of all, one clearly sees the inertial and M2 internal tidal components. Second, one sees a monotonically decreasing section that falls off as f to the minus 1.75. And finally, there is the high frequency part of the spectrum ($\Delta\Omega = 0.8$–10 cph). This last part of the spectrum can be shown to be due to soliton-induced background waves.

It is important to note that in shallow water, the IW field can be strongly anisotropic. The surface manifestations of the IW field are the main evidence we have of this statement. One example of the IW field surface manifestation is shown in Fig. 2.15 for the MAB. This figure presents a mosaic of sea surface images superimposed on a geographic grid. The images were obtained using side-looking airborne radar. The figure clearly illustrates the complexity of the spatial structure of the IW field in shallow water. One easily sees the system of well-pronounced lines, corresponding to the soliton trains, propagating in the onshore direction.

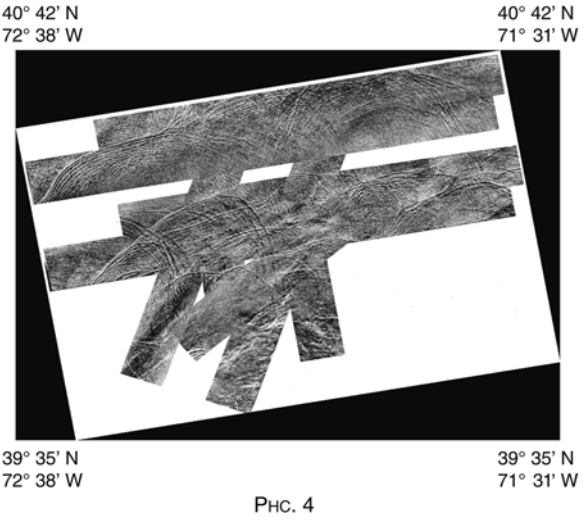


Fig. 2.15 Mosaic of radar images of MAB internal waves

Based on spectral processing of the image, we can see that for this region, the separation between adjacent trains is ~10–20 km and that each train is 1–3 km long. All the trains have an almost plane wave front, with a large radius of curvature of the order 10–20 km. The assumption of a totally plane wave front is usually used for sound propagation simulations in the presence of soliton trains. The spatial spectrum of the image in Fig. 2.15 is presented in Fig. 2.16 (Petnikov et al. 2004). In interpreting this figure, we suppose that the degree of darkness of a small surface element in the photo is proportional to a depth-averaged amplitude of the internal wave (or energy per given area). We see that the maximum of this spectrum is at wavelengths of more than several hundred meters, an expected result. We also see a remarkable anisotropy of the background internal wave field, expected for solitons, but less so for the linear field. This latter result is perhaps not so startling if we note that the soliton train tails consist of linear IW and have roughly the same directional property (including the quasi-plane wave front) as the soliton trains. This clearly demonstrates that the high-frequency background IWs can be induced by soliton trains. Notice that the tidal period internal wave has a well-defined direction and that this wave is the main source of the soliton trains. The monotonic part of the spectrum (see Fig. 2.12) is also formed by the tidal harmonics, and thus we can assume that the IWs in this part of the spectrum propagate in the same direction. Thus, we can state that the background IW of every wave length, except perhaps inertial waves, have the same spatial characteristics and propagate in essentially the direction of the parent soliton train. In describing the anisotropy characteristics of the random background IW field, the directivity function $\Theta(\varphi)$ is usually used. For a single mode assumption (when only the first gravity mode exists), $\Theta(\varphi)$ is equal to

$$\Theta(\varphi) = \int_{-\infty}^{\infty} G_1^s(\tilde{q}, \varphi)\tilde{q}d\tilde{q}, \tag{2.41}$$

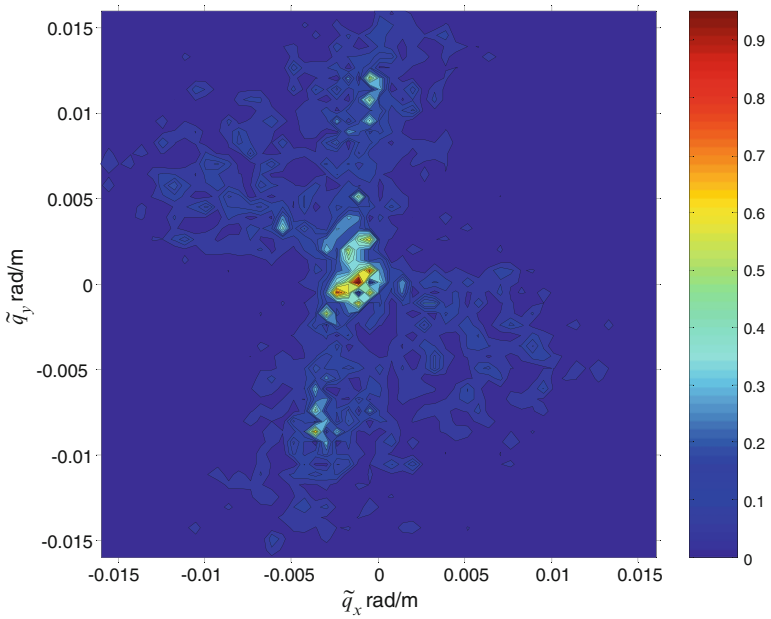


Fig. 2.16 2D (averaged) wavenumber spectrum of IWs

where $G_1^{\mathrm{s}}(\tilde{q}, \varphi)$ is the spatial power spectrum of the background IW field in polar coordinates, and $\tilde{q}_x = \tilde{q}\cos\varphi$, $\tilde{q}_y = \tilde{q}\sin\varphi$. Experimental estimates of $\Theta(\varphi)$ can be made using the radar images of the IW. In doing so, the following assumptions are made:

- The spatial spectrum can be represented as the product of the two functions:

$$G_1^{\mathrm{s}}(\tilde{q}, \varphi) = \tilde{G}(\tilde{q})\Theta(\varphi). \tag{2.42}$$

- Up to a constant factor, $G_1^{\mathrm{s}}(\tilde{q}, \varphi)$ is equal to $G_{\mathrm{si}}^{\mathrm{s}}(\tilde{q}, \varphi)$ for the frequency band $\Delta\Omega$. $G_{\mathrm{si}}^{\mathrm{s}}(\tilde{q}, \varphi)$ is the spatial power spectrum of the surface image of the background IW (without the trains of solitons).

  In this case, $\Theta(\varphi)$ is equal to

$$\Theta(\varphi) = \int_{\tilde{q}_{\min}}^{\tilde{q}_{\max}} G_{\mathrm{si}}^{\mathrm{s}}(\tilde{q}, \varphi)\tilde{q}d\tilde{q}, \tag{2.43}$$

where $\tilde{q}_{\min}$ and $\tilde{q}_{\max}$ are determined by solving (1.98) for frequencies close to the local inertial frequency Ω_i and the buoyancy frequency correspondingly.

Directivity functions for two realizations of the linear background field are plotted in Fig. 2.17 for the IW shown in Fig. 2.15. (The functions are normalized

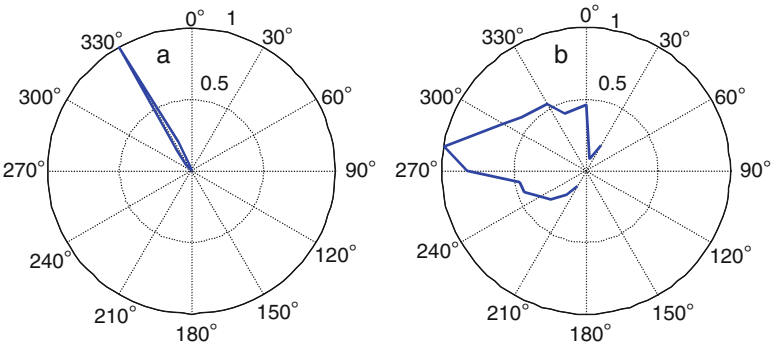


Fig. 2.17 Angular dependence $\Theta(\varphi)$ for the region of the New York Bight in the points 40°23′N 72°30′W (**a**) and 40°13′N 71°47′W (**b**)

here to the maximum value.) For this example, we chose two different areas: one where the IWs have quasi-plane wave fronts (Fig. 2.17a) and one where the wave fronts have a complex form (Fig. 2.17b). As one would expect, the very narrow directivity function corresponds to the IWs with quasi-plane wave fronts, whereas the wave fronts with complex form have a broad beam pattern. Figure 2.17 makes it clear that in shallow water, the background IW field can vary from narrow to broad. This is consistent with our conjecture that the (background) linear internal waves at the tail end of the soliton internal tides leave anisotropic spectra, whereas background waves that are not influenced by the nonlinear field have broader, more isotropic spectra. We note that one also can have areas in the multiple soliton trains going in many directions – in this case, a broad linear spectrum is also expected.

We now turn back to examining the methods of modeling the sound-speed perturbation in the presence of background IW. We can rewrite expressions like (2.32) in a single-mode approximation as

$$\zeta(x,y,z,t) = \int_{\tilde{q}_{\min}}^{\tilde{q}_{\max}} \int_{-\pi}^{\pi} S_1(\tilde{q},\varphi)\Phi_1(\tilde{q},z)\exp\{i(\tilde{q}(x\cos\varphi + y\sin\varphi) - \Omega(\tilde{q})t)\}\tilde{q}d\tilde{q}d\varphi \tag{2.44}$$

where the random field is assured to be statistically homogeneous

$$\langle S_1(\tilde{q},\varphi)S_1(\tilde{q}',\varphi')\rangle = G_1^s(\tilde{q},\varphi)\tilde{q}^{-1}\,\delta(\tilde{q}-\tilde{q}')\,\delta(\varphi-\varphi') \tag{2.45}$$

and $\Omega(\tilde{q})$ is the dispersion relation for the first gravity mode. For estimation of $G_1^s(\tilde{q},\varphi)$, we will assume that the eigenfunction Φ_1 depends only slightly on frequency, or equivalently depends only weakly on the wave number $\tilde{q}$. Note that this is not a strong assumption for shallow water.

Using this assumption, we can write the following simple expression:

$$\left\langle \left|\zeta(\vec{r},z,t)\right|^2 \right\rangle = \Phi_1^2(z)\int_{\tilde{q}_{\min}}^{\tilde{q}_{\max}}\int_{-\pi}^{\pi} G_1^{\mathrm{s}}(\tilde{q},\varphi)\tilde{q}d\varphi d\tilde{q} = 2\int_{\Omega_i}^{N(z)} G^{\mathrm{t}}(z,\Omega)d\Omega, \quad (2.46)$$

where $\left\langle |\zeta|^2 \right\rangle$ is the square of the vertical displacement. Furthermore, by using assumption (2.42) we finally obtain the formula needed for the calculation of $\tilde{G}(\tilde{q})$:

$$\tilde{G}(\tilde{q}) = \frac{2}{\tilde{q}\Phi_1^2(z)} G^{\mathrm{t}}(\Omega(\tilde{q}),z)\frac{d\Omega(\tilde{q})}{d\tilde{q}}\left(\int_{-\pi}^{\pi}\Theta(\varphi)d\varphi\right)^{-1}. \quad (2.47)$$

On the right-hand side of (2.47), one has the physical values which are measured by experiment ($G^{\mathrm{t}}(\Omega,z)$, $\Theta(\varphi)$) or can be calculated via experimental data ($\Phi_1(z)$, $\Omega(\tilde{q})$). Specifically, for the calculation of $\Phi_1(z)$ and $\Omega(\tilde{q})$, we should use (A.98)–(A.100) and the experimental measurement of $N(z)$.

From the above discussion, an algorithm for the computer simulation of a sound-speed perturbation caused by background IWs would be along the following lines:

1. First, generate a 2D, delta-correlated Gaussian random field of vertical displacements $\zeta_\delta(x,y)$ with mean value equal to zero and variance equal to one.
2. Then, calculate the 2D spectrum $S_\delta(\tilde{q}_x,\tilde{q}_y)$ and the corresponding spectrum $S_\delta(\tilde{q},\varphi)$:

$$S_\delta(\tilde{q}_x,\tilde{q}_y) = \frac{1}{(2\pi)^2}\iint_{\tilde{S}}\zeta(x,y)\exp\{-i(\tilde{q}_x x+\tilde{q}_y y)\}dxdy, \quad (2.48)$$

   where $\tilde{S}$ is the area occupied by the internal wave field. We have also used the common knowledge that the random variable $S_\delta(\tilde{q},\varphi)$ has the same statistical characteristics as $\zeta_\delta(x,y)$.
3. Calculate $G_1^{\mathrm{s}}(\tilde{q},\varphi)$ by using (2.47) and the experimental dependences of $G^{\mathrm{t}}(\Omega,z)$ and $\Theta(\varphi)$.
4. Compute $S_1(\tilde{q},\varphi)$ $\left(S_1(\tilde{q},\varphi) = S_\delta(\tilde{q},\varphi)\sqrt{G_1^{\mathrm{s}}(\tilde{q},\varphi)/B_\delta}\right)$, where B_δ is a normalization factor $\left(B_\delta \cong 1/\pi G_{\max}^2\right)$. In this manner, we achieve the relation (2.45).
5. Calculate $\zeta(x,y,z,t)$ using (2.44).
6. Calculate the sound-speed perturbations using $\zeta(x,y,z,t)$.

By way of example, some calculated random realizations of $\zeta(x,y,z,t)$ are shown in Figs. 2.18 and 2.19. Here, we used the spectrum $G^t(\Omega,z)$ shown in Fig. 2.14 and model the dependence $\Theta(\varphi)$ as $\Theta(\varphi) = (\cos\varphi)^n$. Notice that $n = 400$ corresponds to the narrowest directivity function we have seen recorded in an experiment (Kuzkin et al. 2006).

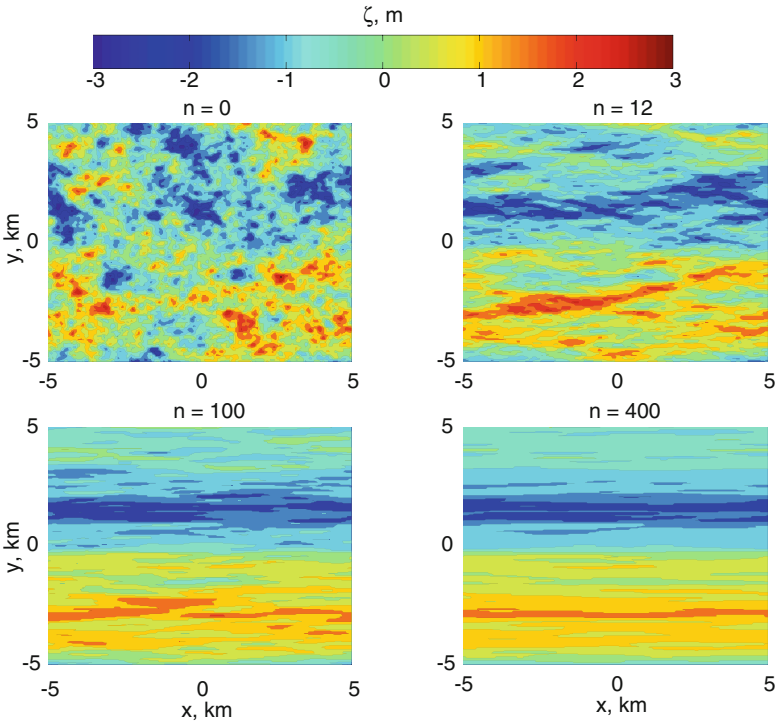


Fig. 2.18 Random vertical displacements at the instant $t = 0$ s, for different values of exponent n of the directivity function (**a**) $n = 0$, (**b**) $n = 12$, (**c**) $n = 100$, (**d**) $n = 400$

2.7 Coastal Geology and Geophysics

The fact that low-frequency sound interacts strongly with the bottom is a defining feature, if not the defining feature of shallow water acoustics. The close proximity (in wavelengths) of the surface and bottom boundaries defines a thin (shallow) waveguide. It is eventually seen that the interaction of the sound with these boundaries is of roughly equal importance to its interaction with the volume (the water column). The effects of the bottom are primarily (1) the reflection of sound, (2) the attenuation of the sound that interacts with it, which dictates the very important propagation loss versus range curve, and (3) the scattering of the sound through rough surface and seabed interior scattering.

It is obvious that in order to understand acoustic propagation and scattering in a shallow water waveguide, one must understand the properties of the bottom. In the following sections, we will discuss these geological properties, especially those most germane to modeling the bottom for acoustics. In that the ocean bottom is both complicated and difficult to measure, the study of the bottom is far from complete at

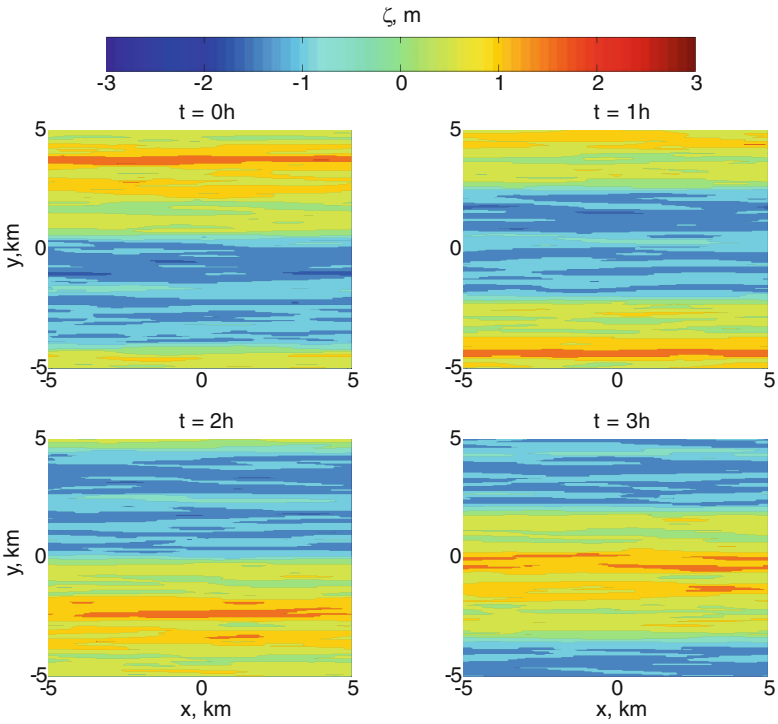


Fig. 2.19 Temporal variation of internal wave field

this point in time, both in terms of geology and acoustics, and so what we will be describing is still a very active area of research (see, e.g., Seibold and Berger (1996) for an overview of the geology).

Shallow water acoustics takes place, by definition, on the continental shelf. The continental shelf is defined as the part of the seafloor that extends from the shoreline out to the shelf break (the latter being the point where there is a large change in bottom slope, leading to abyssal depths). Shelf breaks typically occur at depths of 130–200 m so that the shelf is the relatively flat (with average slopes of less than one degree) area from 0 m to 130–200 m depth.

Shelves can be either broad or narrow, depending on how they formed and what the plate tectonic activity is in their vicinity. A narrow shelf (e.g., the U.S. Pacific coast shelf) can be as narrow as 1 km, whereas a broad shelf (e.g., the U.S. Atlantic coast) can be as wide as 100–200 km, where the distance is measured perpendicular to the shoreline (Table 2.3).

Continental shelves that have little or no seismic activity (“passive margins”) can accumulate sediments over long geological periods and tend to be broad. Shelves which have significant earthquake or faulting activity (“active margins”) that inhibits the accumulation of sediment tend to be narrow.

Table 2.3 Depths and breadths of several oceanic shelves

Place	Average depth (m)	Breadth (km)
Mexican Bight	70	250
Barents Sea	200	1,200
North Sea	180	500
Hudson Bight	100	1,000

Although shelves are considered flat to first order, they often have significant large-scale relief (horizontal scale order of 10 km or more) in areas reflecting (1) water currents that transport sediment in both erosional and depositional modes, (2) the rise and fall of sea level over geological time, (3) glacial scours, and (4) numerous other phenomena. The Hudson Canyon offshore of the Hudson River in New York is a classic example of how geological processes can impose significant bottom relief on an otherwise flat shelf.

The medium scale bathymetry/roughness (horizontal scales of roughly 100 m–10 km) on the shelf will be discussed in detail in a following section, so we will just mention it here.

There is also the "microtopography" (small-scale roughness of order 100 m or less) of the bottom to consider in shallow water acoustics. Though the effect of surface waves in creating bedforms is most significant near the shore, low-frequency surface waves can redistribute bottom sediments at up to 100 m depth, and so the small-scale (bedform) bottom roughness spectrum should be considered a dynamic, changing entity. A useful rule of thumb for determining how small the lateral scale of microtopography one should consider for forward propagation studies is that it be a small fraction (say 0.1) of the acoustic Fresnel zone radius R_F. For a straight line path of distance R connecting a source and a receiver, the Fresnel zone radius is given by $R_F = (\lambda R)^{1/2}$, where λ is the acoustic wavelength (Flatte 1979). For a 100-Hz source transmitting over 20 km (a typical scenario), 0.1 R_F is about 55 m. Scales smaller than this should be looked at as rough surface scattering contributors, whereas larger scales should be treated as bathymetry. This means that a narrow beam echosounder (of order 5° beamwidth) with a bottom patch ensonification width of 10–20 m in 100 m water should be adequate for low-frequency bathymetry surveying, but that as one goes to propagation frequencies near a kilohertz or to closer ranges, the bathymetry map may be undersampled.

Finally, there is the issue of how the surface sediments are distributed on shelves. It is a common observation that the coarsest sediments are deposited nearer to the shore due to the fact that the fall velocity (and thus deposition rate) is larger for large sediments. Thus, the larger terrigenous sediments that are washed into the sea stay near the shore. However, this is a rule with some notable exceptions. First, it is often observed in mid-latitudes that there is a considerable amount of coarse sediment near the shelf break. These are sediments that were transported to the sea from rivers when sea level was lower. (Indeed, sea level has risen some 100–130 m over the past 20,000 years!) They are generally called relict sediments. There is also the case where a river spews forth a large amount of mud and silt,

Table 2.4 A brief précis from Hamilton (1980)

Sediment type	Mean grain diameter (mm)	Density (g/cm^3)	Porosity (%)	Velocity (m/s)	Velocity ratio
Coarse sand	0.5285	2.034	38.6	1,836	1.201
Fine sand	0.1593	1.941	45.6	1,749	1.145
Very fine sand	0.0960	1.856	50.0	1,702	1.115
Silty sand	0.0490	1.772	55.3	1,646	1.078
Sandy silt	0.0308	1.771	54.1	1,652	1.080
Silt	0.0237	1.740	56.3	1,615	1.057
Sand–silt–clay	0.0172	1.596	66.3	1,579	1.033
Clayey silt	0.0077	1.488	71.6	1,549	1.014
Silty clay	0.0027	1.421	75.9	1,520	0.994

Most columns are self-explanatory. The velocity ratio is the velocity in sediment to the velocity in sea water at 23°C, 1 atm, and at the salinity of the sediment pore water

causing a delta or plume offshore of it. The Mississippi, Nile, and Amazon rivers have very famous plumes, with a large amount of fine material close to shore.

The above discussion simply points out that one must seriously consider the geology in trying to understand/predict/measure the sediments in shallow water.

Shelf sediments. In describing the bottom for shallow water acoustic purposes, the main geological entities one needs to ascertain are the bathymetry and the stratigraphy. The bathymetry is, in principle, easily mapped by modern echosounding systems, so we will not belabor it here. The stratigraphy, which includes the layering of the sediments, their types, their age, their mode of deposition, and their geographic extent, is a more challenging study, and indeed is one of the significant open problems in shallow water acoustics. We will first look at the types of sediments found in shallow water in this section, before turning to layering structure and other necessary parts of the stratigraphic record.

Though over a quarter-century old, one of the most useful papers in the ocean acoustician's collection is Edwin Hamilton's "Geoacoustic modeling of the sea floor" (Hamilton 1980). This paper contains much of the basic information one needs to create simple first-order acoustic models of the seabed in a wide range of locations, including our prime area of interest, the continental shelf. Two of the most useful items in this paper describe continental terrace (shelf and slope) sediment properties, which we paraphrase in Table 2.4. The numbers in these tables show what types of sediments are dominant on the shelf (sands, silts, and clays, in various combinations), their sizes (from larger sand grains to fine silty clay particles), three principal geoacoustic properties (the density, sound speed, and the water–sediment interface sound-speed ratio), and two prime poro-elastic medium properties (the mean grain diameter and the porosity). The entries in this table are, to repeat, first-order estimates, but they provide a good starting point for more refined bottom models.

Though the acoustic properties of these sediments are probably already familiar to the reader, we briefly note them anyway. It is seen that there is an increase in

sound speed and density as one goes from the softer, smaller sized sediments (muds and silts) to the larger sediments (sands). Moreover, the velocity ratio increases in the same way as one goes to larger sediments. One of the more interesting entries in this table is the velocity ratio for silty clay, which is less than one, and indicates that the near-surface sediment actually creates a low speed acoustic duct in this case (e.g., see Frisk 1994).

We note, at the risk of triviality, that this table is somewhat incomplete. It omits the calcium carbonate sediments that one gets at low latitudes from coral remnants, the larger pebbles (and even rocks and boulders) one gets from glacial debris at higher latitudes, shell hash that is common on all shelves, and other contributors.

Knowing what sediments are found on the continental shelf in a general sense is not sufficient to give one the precise knowledge that is needed to understand acoustics at a given site. To do this, one needs to know the local sediment types and their variation with depth down to (as a rule of thumb) 2–3 acoustic wavelengths into the sediment. Thus for 100-Hz propagation, one would like to have the properties of the top 30–45 m into the sediment. It is relatively easy to ascertain the properties of the surface sediments via grab samples, cores (box, piston, etc.), accelerometer impact probes, surface reflectivity surveys, photographs, etc. However, sampling deeper sediments becomes problematic. Coring or other such direct probing is the only foolproof way to identify subsurface material, and even this can be difficult. Long cores of near-surface sedimentary material are harder to get on the shelf, particularly in regions with noncohesive sands, where obtainable core lengths may only be a few meters.

One might argue that acoustic probing could be used to get at the type of subsurface material, but this is also difficult, as acoustic profiling primarily senses impedance (the product of density and sound speed), which can be an ambiguous measurement of material type.

Vertical layering and horizontal structure of shelf sediments. In addition to the material type of the sediment, one also needs to know the layering structure of the sediment for acoustics purposes. This component of the problem is what most people commonly think of as "stratigraphy," as it is the direct description of the layers or strata. A typical stratigraphic section of interest to shallow water acoustics is shown in Fig. 2.20. This low-frequency echosounder image shows sloping layering, remnant riverbeds, cut and truncated layers, and other interesting structure that goes well beyond the "simple horizontal stratification" ansatz that is often invoked in modeling the shallow seabed.

2.8 Acoustics of Sediments

In the science of stratigraphy, geologists use the chemistry (especially radiochemistry), the biology (e.g., skeletal fragments), the physics (e.g., magnetics, fluid properties, etc.), and the geometry (the strata and their discontinuities) of rock

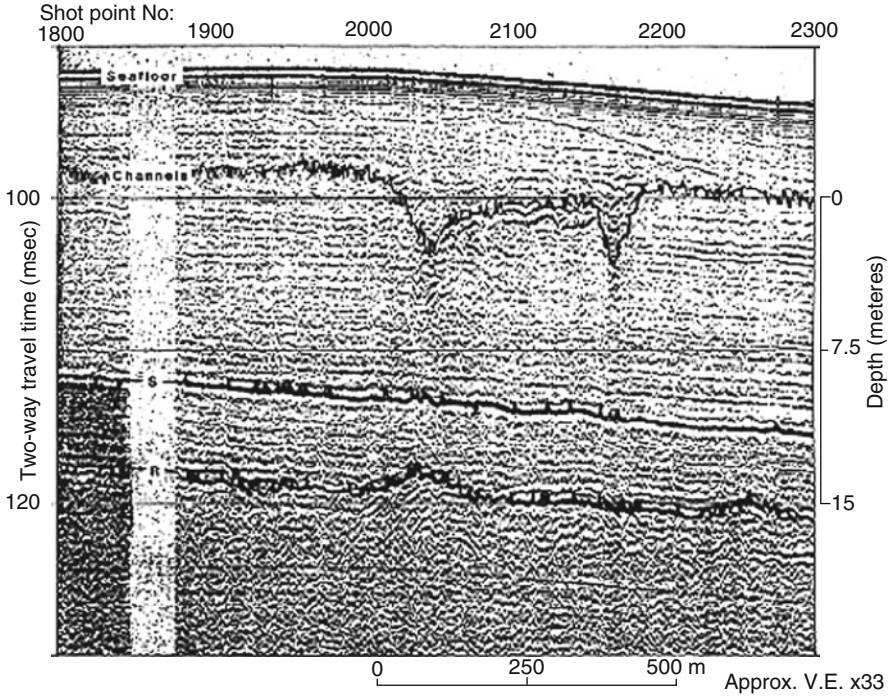


Fig. 2.20 Stratigraphic section from off the coast of New Jersey, showing seafloor, remnant river channels, and the so-called R and S stratigraphic interface reflectors. From Carey, IEEE JOE

and sediment layers as clues in the scientific detective story of the history of the Earth and planets. This is a subject of enormous interest, and indeed the progress over the last century in this area has been staggering.

However, from the pragmatic viewpoint of a shallow water acoustician trying to obtain the acoustic properties of the lower waveguide boundary, the full science of stratigraphy is simply "too much information." What acousticians mainly need is a much simpler thing – the sound-speed, density, and attenuation profiles in the seabed which are (again, to first order) primarily a function of depth. Thus, we will look at this 1D model first and then return to geological stratigraphy (e.g., Fig. 2.20), which will provide the full 3D corrections to the simplified model.

We will look here at two representatives of the acousticians "simplified view" of continental shelf stratigraphy (1) the vertical region model of Hamilton (1980) and (2) the three-region model presented by Katsnelson and Petnikov (2002).

Hamilton's treatment of how to create sediment geoacoustic models is epitomized in his Appendix A, "An example of a geoacoustic model," in which he creates an Abyssal Plain bottom geoacoustic model. While abyssal environments typically have a thick layer of soft sediments compared to shallow water shelf environments, the use of regression equations (based on physical principles, laboratory, and field data) to create vertical sound-speed, density, and attenuation

profiles, and the breaking of the profile into the three regions of (1) sediment, (2) sedimentary rock, and (3) basement are a basic methodology in bottom acoustics. Indeed, Hamilton's work is some of the earliest and most influential in this field, and it is acknowledged that much of the later work in the field builds upon his lead.

As an example of work that builds upon the "Hamiltonian framework" (with due apologies to the physics community), the simple Katsnelson and Petnikov model (see Fig. 2.1) prescribes that coastal sediments have three distinct vertical regions (1) a top layer of unconsolidated sediments, describable by a simple fluid model, of order 10-m thick; (2) a layer of semiconsolidated sediments, extending from 10 to 100 m depth, and also described by a fluid model; and (3) a basement of consolidated sediments, for which solid, elastic medium properties may be important. Sound velocity profiles (and density and attenuation, which we will leave tacit from here) in these regions are based on the material composition of the sediments and are computed from regression equations such as Hamilton's while incorporating any other available historical data, such as cores or acoustic surveys. There may or may not be a discontinuity in sound speed between layers I, II, and III. Layer thicknesses are also somewhat adjustable.

In constructing vertical sound-speed profiles as per the above prescriptions, we note again that we are not using three isovelocity regions, but rather three sediment type regions, each of which has a variable (and not necessarily continuous) vertical sound-speed profile. In describing this with a layered model, we are thus invoking an N-layer model, where N is infinitely large in the limit.

Let us now look at an example of a shallow water geoacoustic model, using some work by Lynch, Frisk, and Rajan off Corpus Christi, Texas (Lynch et al. 1991). Interestingly, one of the motivations of this work was to see how well an a priori geoacoustic model created from high-quality historical data, Hamilton's regressions, etc., could predict newly measured low-frequency acoustic transmission loss data. The a priori model for compressional wave speed and the acoustical inverse model inferred are shown in Fig. 2.21. It is noted that the acoustic inverse result and the a priori data model are different, even though the acoustic inverse model provides an excellent "best least squares fit" to the acoustic transmission loss data, as does the a priori data. This is simply a reflection of the fact that the historical model and the acoustic inverse result have very different vertical resolutions, with the historical data in fact having the better resolution in this case. This is particularly evident at sharp interfaces in the sediment. This simple intercomparison of two "good quality" bottom geoacoustic profile estimates brings out an important point. That is, in creating a "best" bottom model, one needs to pay careful attention to the resolution, variance, and bias of the measurement and model components that make up the estimate. A weighted average that keeps the best pieces of all the component data is what should be used.

One or two more details should be noted on the resolution available, using the Corpus Christi data. First, we see that the historical geological data, which includes core data (with very high vertical resolution, of order centimeters) and high-frequency vertical echosounder data (order $\Delta z = c\tau/2$, where τ is a pulse length on the order of a millisecond, thus giving $\Delta z \sim 1$ meter), give a far better look at the sharp, subsurface

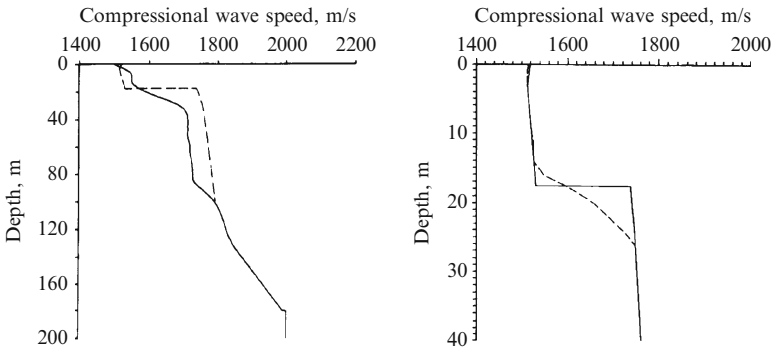


Fig. 2.21 *Left panel* shows an intercomparison of a high-resolution compressional wave speed profile ("Matthews model," *dashed line*) and the result of a low-frequency acoustic inverse (*solid line*). It is seen that the LF inverse shows smoother interfaces versus depth. The *right panel* shows the result of looking at a specific sharp interface ("Matthews model," *solid line*) with only low-frequency acoustic data, i.e., the smoothing of the interface. In this panel, the sharp profile (*dashed line*) is convolved with the vertical resolution kernel of the low-frequency inverse to produce the smoothed result. From Lynch et al., JASA

interfaces that were encountered. This is because the low-frequency acoustic data (a $p(r)$ vs. r data set used for a Hankel transform inverse) have vertical resolution in the bottom given by the differences in turning points (or e-folding lengths) of a sparse set of normal modes, of order ~1 m near the surface and 10 s of meters deeper down. However, near the surface, the LF acoustic data set actually was the better descriptor, in an interesting way that one might not think of, namely, in the temporal dimension. The LF acoustics was able to see a change in the near-surface sound speed due to the change in temperature of the pore water with season, an effect that was not resolved in the historical data (Rajan and Frisk 1992).

The simplified view of bottom modeling described above was sufficient for shallow water acoustics for a number of years, and indeed is still sufficient for many applications today where only modest accuracy is needed. However, both coastal geology and shallow water acoustics have "gone to the next level" of sophistication, namely, a fully 3D medium description, and so we should look at what these recent advances have added to our ability to model the bottom in shallow water. Let us start from the geology viewpoint.

The first thing an ocean acoustician realizes when looking at a 3D geological description of the continental shelf sediments is that he or she is in a whole new world which speaks an entirely different language. Instead of "geoacoustic model" or "sound-speed profile," one sees vocabulary like stratigraphy, morphology, lithology, sequences, facies, strata, tracts, regressive and transgressive sequences, and lowstand and highstand systems. In addition, one encounters the geologic time scale names like Holocene epoch, Quaternary period, and Cenozoic era (all three of which we belong to!). To add to the acoustician's confusion, one finds that, until rather recently, most geological stratigraphy studies were made with low-frequency seismic arrays, which have rather poor resolution of the near-surface sediments

(e.g., the top 100–200 m) which are of most interest to shallow water acousticians. Thus, one can easily get discouraged in trying to translate the geologist's findings into acoustical terms – which would be too bad, as the more recent work in geology has a lot to tell the shallow water acoustician.

Unfortunately, there is no "quick fix" to introducing geology to acousticians; rather, we will make the recommendation (which also holds for physical oceanography and biology, two other marine science areas with strong acoustic links) that the modern ocean acoustician should invest the time needed to get an overview of those areas, at least at the level of an introductory course. Modern ocean acoustics is more and more concerned with detailed effects of the 3D transmission/scattering medium, which come directly from geology, physical oceanography, and biology. Again, we might recommend two basic texts, which the reader can then supplement from his or her own topical interests. They are (1) "Marine Geology" by Kennett (1982) and (2) "The Sea Floor" by Seibold and Berger (1996).

However, even a rudimentary knowledge of geology is still not enough to translate geology to acoustics – one rather critical piece is still missing, namely, what geoacoustic description of a geologically complex medium is adequate/reasonable/usable/etc.? We are now endeavoring to go beyond simple 1D horizontally stratified seabeds (where the sound speed is only a function of z) to a fully 3D seabed. How one describes a 3D geologic/geoacoustic field is still an interesting question, so we see that we have two problems to solve (1) translation of the geologist's map into acoustic variables and (2) a "reasonable" way to express a complicated 3D field of variables for use by acousticians.

By way of example of a modern 3D dataset, let us look at a recent research result from a combined watergun, chirp sonar, and core survey of a section of the East China Sea that was obtained as part of the 2000–2001 Asian Seas International Acoustics Experiment (ASIAEX). Two color plots showing (a) the surface sediment layer thickness for the area and (b) the thickness of the layer just underneath the 0–3-m sandy sediment layer are presented in Figs. 2.22 and 2.23, taken from Miller et al. (2004). The nomenclature "surface layer" from the article is the same as the acoustics usage, so the cross-disciplinary translation is not a problem. The discussion in the article then describes the second layer as "the difference between the transgressive systems tract depth and the sequence boundary," but it is clear that this is a "second layer" in acoustics terms. Thus, the geology-to-acoustics translation is perhaps not as hard as it seems, at least for this case.

The sediment maps in Figs. 2.22 and 2.23 give a top view of the sediment's complexity, just as Fig. 2.20 gives a side view. A spectral/correlation analysis of the ASIAEX data by Abbot, Dyer, Emerson (2006) shows that both layers have roughly isotropic wavenumber spectra, but different correlation lengths, i.e., 2 km for the top layer and 4 km for the bottom layer. Figs. 2.22 and 2.23 make it clear that the structure of shallow water sediments can be complicated.

We will next look at how we describe such complicated structure, i.e., the solution to the "geoacoustic model/description" problem. It is apparent that storing the complete set of 3D geoacoustic parameters at every spatial point is overly computer memory intensive and awkward. Thus, a more compact solution should

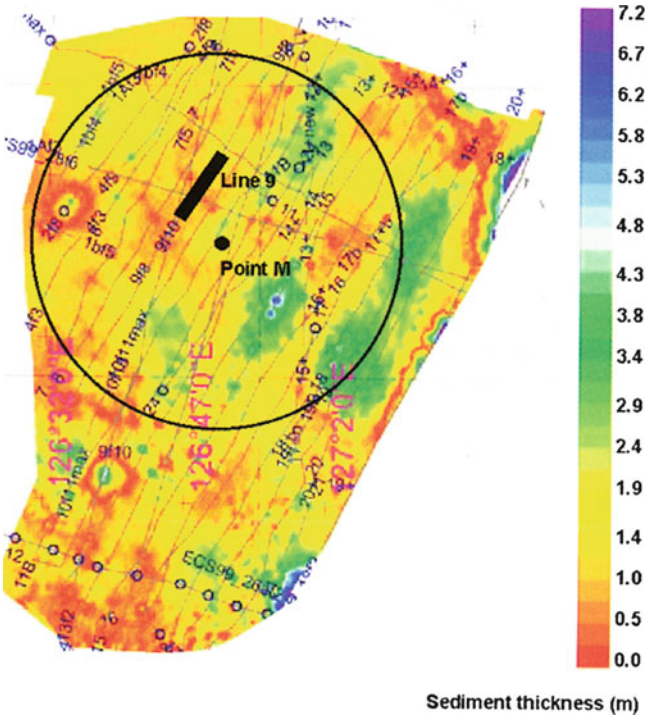


Fig. 2.22 Surface sediment layer thickness (m) at the ASIAEX East China Sea experimental site, inferred from a survey made by L. Bartek. Miller et al. (2004) (with permission from IEEE)

be sought. Three possible solutions come quickly to mind (1) a low-pass filtered layer boundary map, (2) a power spectral (or equivalently autocorrelation function) representation of rough layer boundaries, and (3) an EOF representation. All these have their strengths and weaknesses, which we now discuss.

If one is interested only in a smoothed representation of the bottom layering (range dependence), then it is a simple task to low-pass filtered 2D layer thickness maps, such as those in Figs. 2.22 and 2.23, and store the numbers on a regular grid. This approach is computationally easy but has two weaknesses. First, it (obviously) ignores the high-frequency horizontal variability of the sediments and second, it assumes that the layers maintain their identity (material properties and position relative to each other) over the region mapped. This latter assumption is the one most likely to be violated in shallow water, where the geology is complicated and individual layers can appear or disappear.

The second way of mapping the sediment layering is really an extension of the first, where one superposes some roughness upon the smooth map of #1, using the data to derive an appropriate power spectrum. This is also a computationally tractable way of representing the data. It has the added advantage that one can calculate some of the finer scale scattering effects from the bottom, using the

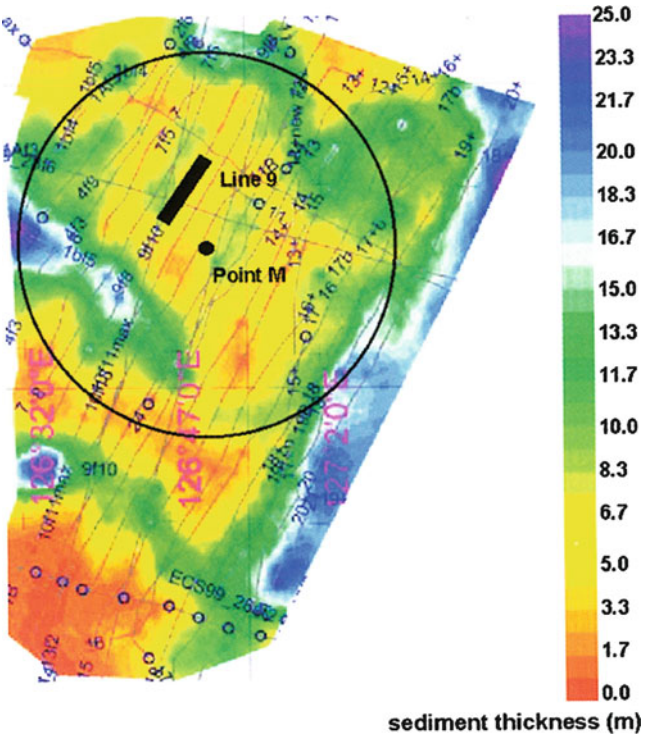


Fig. 2.23 Layer two sediment layer thickness (m) at the ASIAEX East China Sea experimental site, inferred from a survey made by L. Bartek. Miller et al. 2004 (with permission from IEEE)

realizations of either the roughness or the acoustic power equations. It has the disadvantage that the power spectrum loses the phase of the signal, which in this case means it does not reproduce the true realization of the finescale layering structure at a given site. If one does not need the exact finescale regional layering structure, this is adequate. This method also has the weakness of #1 in that it assumes that the layers maintain their identity. We will give an extended discussion of this approach in the next section.

The third method of dealing with bottom layering structure is to use empirical orthogonal functions, which are also discussed in the context of creating useful maps of fully 3D water column oceanography. The advantage of this technique is that it creates a map with the best fidelity to the local region, i.e., it maintains the proper layering structure, including any discontinuities. If one needs the exact local structure, the EOF representation allows one to get precisely the right answer at the data points and also provides the ability to interpolate between them in simple and sensible ways. The major flaw with the EOF representation for the bottom structure is that it is best suited to a red spectrum (like the ocean water column structure). When applied to the bottom, it is seen (J. Miller, private communication) that many modes need to be kept in order to account for most of the variance. This makes the

field representation by EOFs far less economical than for the oceanography; however, the fidelity and the added ability to interpolate the data perhaps compensate for this.

In considering the detailed layering of the bottom sediment, there is also the interesting observation that a number of fine, thin layers can (for some purposes) be replaced by a larger "effective layer" (Avseth et al. 2005). This replacement of fine structure by larger scale "effective structure" is an interesting, and still not fully explored, area in ocean acoustic research.

We should also note that the above discussion does not constrain the properties of the layered medium. One can use a fluid model, solid model, poro-elastic model, etc. Moreover, in all these methods, extrapolation outside the measurement region can only be trusted out to a horizontal and vertical correlation length. Past there, one should revert to the mean-layering profile.

There are other possible representations of the bottom stratigraphy that we have not explored here, e.g., fractal representations. (Fractal roughness will be treated in a later section.) We do not claim to have exhausted the possibilities here; rather, we have just shown a few reasonable ones.

The final topic we will discuss in this section is the implications of this work for both "useful descriptors" of bottom layering and inverse models. The question of "how many local layers (at a given x, y geographical coordinate, since we are now looking at 3D) are adequate," both for the acoustics calculations one wishes to do and to explain the data one takes, is an interesting and important one. The first problem is actually easy enough to address via a sensitivity study. If one is interested in predicting some aspect of the acoustic field, e.g., the magnitude of the pressure field as a function of range for a given acoustic transmission frequency, one can do a sensitivity study that varies the number of layers of the "real bottom" and then judge what number of layers gives adequate resolution for the task at hand. This can be done by averaging layers over some vertical scale, eliminating deeper layers ["hidden depths" (A. Williams 1970)], etc. In the horizontal, one should estimate what the effects of diffraction are to see whether or not to eliminate or consolidate layers.

On the contrary, the question of how many (local) layers are appropriate for an inverse calculation is a different issue. In doing an acoustic inverse (the process of which will be discussed in detail later), one is generally facing an under-determined problem when trying to determine the vertical profile of a given geoacoustic property (e.g., sound speed) at a given geographical point. A common tactic used to address this is to break the local vertical profile into N thin layers, where N is large, and then solve for the property in each layer, using the inverse constraints (e.g., best least squares fit to the data and minimum norm solution) to eliminate the under-determinedness. While this supplies a solution (a number) at every layer depth, these layers are not necessarily resolved by the inverse. Indeed, one needs to look at the vertical resolution kernel of the inverse to find out just how many real (resolved) layers inversion of the data will support. One way to do this is to propagate the layers down from the surface using the resolution kernel the inverse provides. For instance, if near the surface, the resolution length is 1 m, and below

that it is 10 m, and below that it is 10,000 m; we are probably justified to make a three-layer model (the bottom layer being an effective infinite half-space) with interfaces at 0 m, 1 m, and 10 m. What the resolution is versus the depth into the bottom will depend on the dataset used. For instance, given a combination of low-frequency acoustic data and 3.5-kHz vertical echosounder data, the resolution may be better modeled with a different set of layers than for just the low-frequency data alone. Our main points in this last discussion are (1) the layering used in creating a model should be dictated by the vertical resolution of the data available and (2) creating such layered models is still somewhat of an art form, and the answer forces should be dictated by the user's needs.

2.9 Bottom Roughness

In considering bottom properties in shallow water, bottom roughness is certainly another important issue. In this section, we take the phrase bottom roughness to operationally mean the random perturbation of ocean depth $h(r)$ with typical horizontal and vertical scales 10–1000 m and 0.1–30 m, respectively. Other operational scales are also usable, and we should quote the old ocean acoustics joke "one man's roughness is another man's bathymetry." As previously noted, the acoustic frequency used and Fresnel radius/bottom footprint are the practical determinants of this boundary. Mathematically, we assume that depth can be represented as a sum of two terms $H(r) + h(r)$, where $H(r)$ is the macroscale bottom contour, which can be considered as a deterministic process in comparison with $h(r)$.

It should be noted that in shallow water, there exists bottom roughness with smaller horizontal and vertical scale, which is the result of the transport of sediments (Trowbridge and Nowell 1994). However, these microscale roughness elements do not have much effect on low-frequency sound propagation on continental shelves, and so will be ignored for the remainder of this discussion. (At medium frequencies, these scales can be important, however.)

We now look at the bottom roughness in a spectral/correlation function approach. As a first approximation, $h(r)$ can be considered as a stationary, anisotropic, zero mean, Gaussian random field completely specified by its two-point correlation function (Goff and Jordan 1988)

$$B_h(\vec{r}) = \sigma_h^2 \Phi(\hat{r}(\vec{r}))/\Phi(0), \tag{2.49}$$

where σ_h is root mean square (RMS) depth variation, $\Phi(\hat{r}) = \hat{r}^{\nu} K_{\nu}(\hat{r})$, K_{ν} is a modified Bessel function of the second kind and order ν, and $\hat{r} = \sqrt{\hat{q}_{11}x^2 + 2\hat{q}_{12}xy + \hat{q}_{22}y^2}$, where $\hat{q}_{ij}$ are the Cartesian elements of a positive-definite, symmetric matrix $\mathbf{Q}$ and have dimensions of $(\text{length})^{-2}$. $\mathbf{Q}$ is expressed in terms of its ordered eigenvalues $\hat{k}_n^2 \geq \hat{k}_s^2$ and its normalized eigenvectors $\vec{e}_n$ and $\vec{e}_s$ which are orthogonal to each other, i.e.,

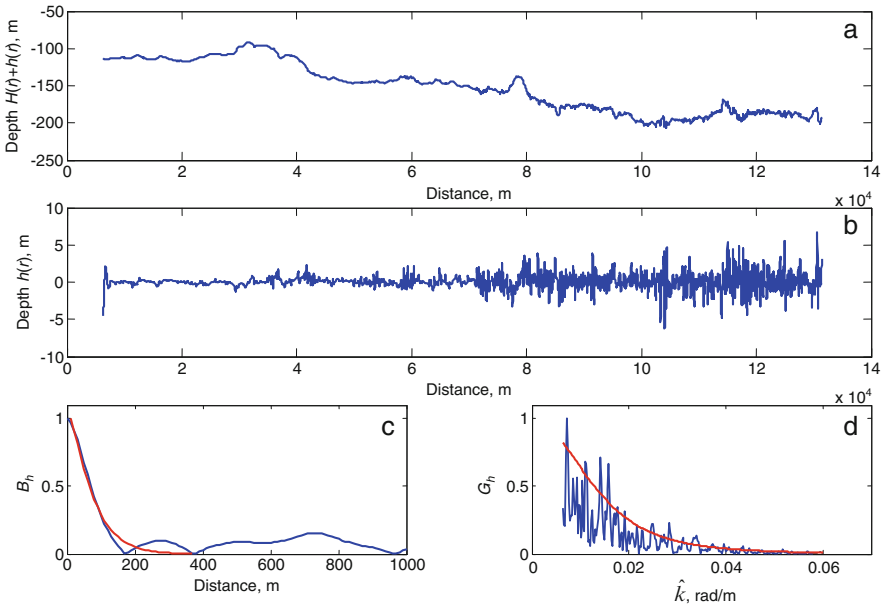


Fig. 2.24 Bottom roughness recorded in Barents Sea. (**a**) $H(r)$+$h(r)$, (**b**) $h(r)$, (**c**) and (**d**) correlation function of random field $h(r)$ and its spatial power spectrum (*blue lines*), respectively. Correlation function (**c**) and power spectrum (**d**) calculated in accordance with (3.1) and (3.4) are shown by *red lines*. All correlation functions and power spectra are normalized to the maximum values

$$\mathbf{Q} = \hat{k}_n^2 \vec{e}_n \vec{e}_n^{\mathrm{T}} + \hat{k}_s^2 \vec{e}_s \vec{e}_s^{\mathrm{T}}. \tag{2.50}$$

Notice that $\hat{k}_s$ characterizes the correlation radius of the random field $h(r)$ in the horizontal direction, determined by the azimuth φ_s. This direction corresponds to the smaller characteristic wavenumber $\hat{k}_s$. The characteristic values define an aspect ratio

$$\widehat{a} = \widehat{k}_n / \widehat{k}_s, \tag{2.51}$$

which is unity for the case of an isotropic random field.

In accordance with (A.28) of our reference, the spatial power spectrum of bottom roughness is equal to

$$G_h(\hat{\vec{k}}) = (2\pi)^{-1} \nu \sigma_h^2 |\mathbf{Q}|^{-1/2} \left[u^2(\hat{\vec{k}}) + 1 \right]^{-(\nu+1)}, \tag{2.52}$$

where

$$u(\hat{\vec{k}}) = \left[\hat{\vec{k}}^{\mathrm{T}}\mathbf{Q}\hat{\vec{k}}\right]^{1/2} = \sqrt{\left(\hat{k}/\hat{k}_s\right)^2\cos^2(\varphi-\varphi_s) + \left(\hat{k}/\hat{k}_n\right)^2\sin^2(\varphi-\varphi_s)}. \quad (2.53)$$

In practice, the parameters found in (2.49) through (2.53) are characterized by strong geographic variability. As an example, in Fig. 2.24a, b we show the bottom roughness recorded in one of the regions of the Barents Sea. The RMS value was equal to $\sigma_h \approx 1\,\mathrm{m}$. The corresponding correlation function and spatial power spectrum are also plotted in Fig. 2.24c, d, as the functions $B_h(r)$ and $G_h(\widehat{k})$ calculated by using (2.49) and (2.52) with $\hat{k}_s = 0.02$. Since we did not have data concerning the anisotropy of the roughness field (which in general one does not), we assume in this calculation that the $h(r)$ shown in Fig. 2.24 is isotropic, i.e., $\hat{r} = r$ and $a = 1$. We also assume that[2] $\nu = 1$. As can be seen from Fig. 2.24, the model matches the experimental spectrum and correlation function more or less reasonably. We note that the correlation distance of bottom roughness shown in Fig. 2.24c is equal to $L_r \cong 1/\hat{k}_s = 50\,\mathrm{m}$.

The data in Fig. 2.24 also display some obvious spatial nonstationarity (e.g., the high wavenumber roughness increases with the range), demonstrating some of the pitfalls in imposing "simple" processing on a complicated ocean bottom.

2.10 Solid and Multicomponent Layered Bottom Models

In the previous sections, we considered the bottom as a multilayered fluid medium. A more realistic and, naturally, more complex model for the bottom is the so-called multilayered elastic solid bottom model (a single-layer elastic solid bottom model being a first approximation). In this model, two types of waves dominate (1) the compressional wave, which is the usual longitudinal acoustic wave that we have studied in fluids, and (2) the shear wave, which is a transverse wave that can exist only in a solid medium. The linear elastic medium is, in the most basic form, described by Hooke's law, which is a tensor equation relating the stress tensor (the imposed forces on the solid) to the strain tensor (the resulting deformation of the solid). For an isotropic, linear elastic medium, only two constants are needed to specify the stress–strain relation completely. The two most usual are the Lame coefficients λ, μ (Mavko et al. 2003; Brekhovskikh 1980). Other possibilities are the bulk modulus, Young's modulus, and the P-wave modulus. We refer the reader interested in the various forms of Hooke's law to the above references, which are two among many.

[2] Notice that parameter ν connected with Hausdorff (fractal) dimension D of the stochastic process $h(r)$ is $D = 3 - \nu$. For the sea bottom, D generally lies in the range from 2 to 2.5 (Goff and Jordan, 1988).

Table 2.5 Geoacoustic properties of elastic solid bottom material typical of shallow water

Sediment	Density (g/cm^3)	Speed of longitudinal waves c_l (m/s)	Attenuation coefficient of longitudinal waves α_l (dB/m kHz)	Speed of shear waves c_s (m/s)	Attenuation coefficient of shear waves α_s (dB/m kHz)
Aleurite–clay, mud	1.9	1,520–1,600	4–10	300–600	
Chalk	2–2.2	2,000–3,000	0.8–1	400–1,500	0.1–4
Basalt	2.3–2.5	3,000–5,000	0.02–0.08	1,600–2,500	0.02–0.1
Coarse sand	2.0	1,800	0.47	250	

Within the framework of the geoacoustic model, we characterize an elastic bottom by five geoacoustic parameters: density, compressional (longitudinal) wave speed and attenuation, and shear (transverse) wave speed and attenuation. The speeds of the compressional and shear waves can be expressed through the Lame parameters as

$$c_l = \sqrt{\frac{\lambda + 2\mu}{\rho}}, \; c_s = \sqrt{\frac{\mu}{\rho}}. \tag{2.54}$$

In order to get a feel for the solid bottom parameters of sediments in shallow seas, we present Table 2.5.

At this point, one has to decide whether to "take the plunge" into the depths of elastic media theory or to expend one's efforts elsewhere. For the purposes of shallow water acoustics, we would generally advise the latter course, not out of laziness, but because of the numbers presented in Table 2.5. Specifically, one notes that in the sands, clays, and silts that dominate the bottom material in shallow water, the shear wave speed is rather low. Only in chalk (e.g., carbonate coral reef material) or basalt (rock bottoms, as opposed to sediments) does one see high shear speeds. We will show below that only for high shear speeds (i.e., less usual bottom material) does one need to include shear effects in a detailed manner.

Our argument is based on Fig. 2.25, which is taken from the text by Brekhovskikh and Lysanov (1991). In this figure, one sees that for shear speeds typical of sands, clays, and muds (like curve 3), the effects of shear on the magnitude of the plane wave reflection coefficient are comparatively small. This means that we might be able to account for shear effects by some sort of perturbation to the compressional wave problem, and indeed we consider just that in a later section of this book. Specifically, shear provides an effective attenuation mechanism for the compressional wave, which converts partially to shear wave energy, which is then lost quickly in the sediment.

Next, we will note that there are also interface waves (Scholte waves) that are created by the existence of shear in the bottom sediments. These can be useful in obtaining bottom shear properties, and again we refer the reader to Brekhovskikh and Lysanov (1991) for further details.

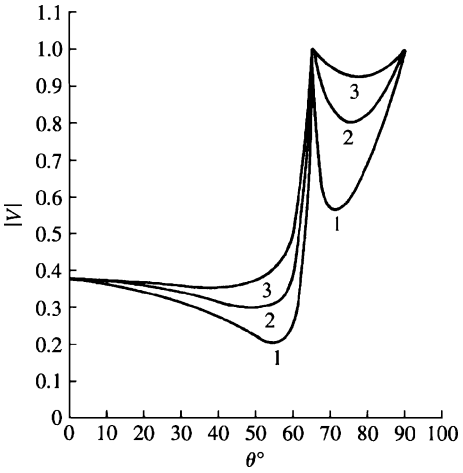


Fig. 2.25 Magnitude of the reflection coefficient for three different bottom shear speeds. For curve 1, $c_s = 750$ m/s, for curve 2, $c_s = 600$ m/s and for curve 3, $c_s = 450$ m/s. Bottom density is twice water and sediment compressional wave speed is 1,666 m/s. From Brekhovskikh and Lysanov. θ° is angle of incidence

In closing this section, we will try to make some amends to the reader for not treating the cases where the bottom material has a high shear speed, e.g., carbonate and basaltic bottom. Many good references on the topic exist, and we would refer the reader to the texts by Brekhovskikh, Jensen et al., and Mavko et al. as good starting points. The theory of linear elastic media is well developed, understood, and implemented (via computer models) at this point in time so that the reader can expect a reasonably good answer to any questions about these effects.

Multiphase bottom models. It is obvious to anyone who has ever walked on a sandy beach washed by waves (the swash zone) or who has trod on the bottom of a muddy bay or silty river that the bottom sediments in the ocean are not pure solid or pure liquid, but rather a two-phase mixture. The question then arises how does this mixture behave compared to the pure liquid or pure solid cases that we have considered so far? Rather luckily for ocean acoustics, the study of poro-elastic media has been pursued for many years by the soil mechanics and groundwater hydrology communities, who are interested in buildings and structures being placed on such media, reservoir behavior, and other such practical engineering problems. Thus, a body of literature applicable to the ocean bottom existed long before ocean acousticians needed to refine their fluid and solid models of the bottom.

One of the most well-known poro-elastic medium theories is the so-called Biot theory, which is also often called the Biot–Stoll theory, acknowledging the significant extensions of the theory by Stoll (1989). We will discuss some of the background and the modern uses of this theory in shallow water in the next section, but first we would like to show just *why* we need to go to this next level of sophistication in modeling the seabed. We will first look at theory predictions and then at experiments to provide this justification.

Our theoretical bolster for looking at poro-elastic media comes from the work of Stoll (1989). In Figs. 2.26 and 2.27, we show (respectively) the compressional wave

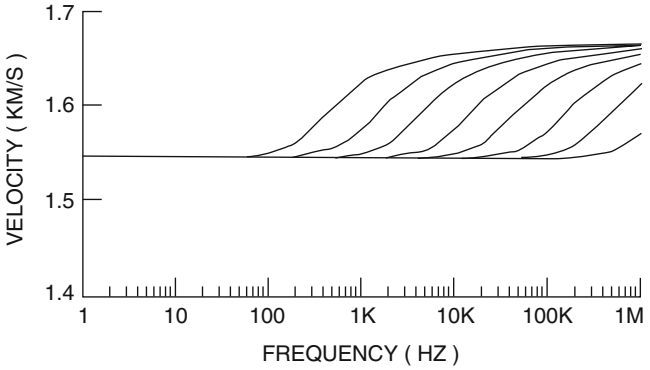


Fig. 2.26 Biot–Stoll model velocity dispersion curve

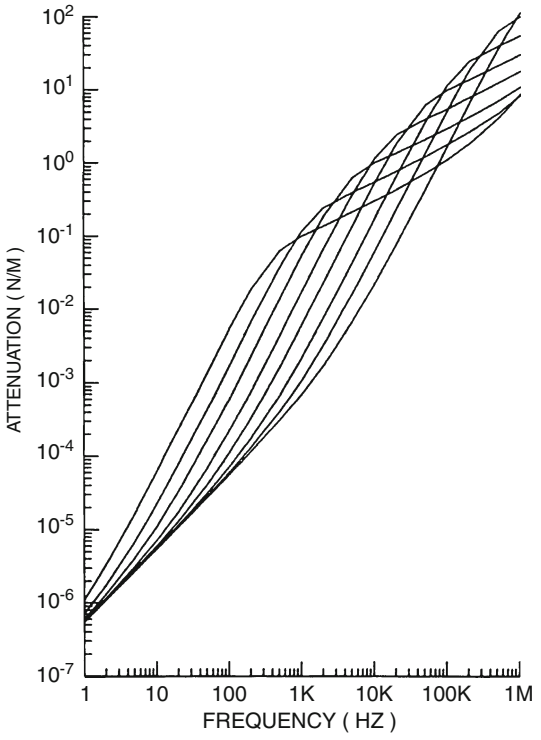


Fig. 2.27 Biot–Stoll model attenuation dispersion curve

velocity and compressional wave attenuation versus frequency. In Fig. 2.26, we see that the Biot–Stoll theory predicts *dispersion* (frequency dependence) of the medium sound speed, an effect that does not occur in either the pure liquid or solid cases. In Fig. 2.27, we see variability in the power law for attenuation versus frequency, something which does not happen for the simple liquids or solids, which

predict only linear frequency dependence. It is thus obvious that poro-elastic theory is predicting effects that are not seen in the simpler theories, and so we should now try to see if such effects are observable by experiment. (Before leaving the curves in Figs. 2.26 and 2.27, we should note that the different curves in each feature represent given variations in the parameters $\widehat{\alpha}$ (the pore size parameter) and $\widehat{k}$ (the coefficient of permeability) in such a way that $\widehat{k}/\widehat{\alpha}^2 = \text{constant}$.)

We now look for experimental evidence of poro-elastic medium effects. In looking for these, we can examine either compressional wave effects or shear wave effects. As shear waves are hard to measure in sediments, we prefer to look at compressional waves. We have the choice of the real part (sound speed) or the imaginary part (attenuation) to consider, or both. Present theoretical predictions of poro-elastic soundspeed dispersion effects show that the signal sizes should be only a few tens of meters per second in real marine sediments. While measurable, this is small and often masked by experimental error, so we should thus turn to compressional wave attenuation. Luckily, in this case, the signals are *not* so small, as we shall see.

As mentioned, the simple fluid and elastic models predict a linear attenuation dependence with frequency, whereas poro-elastic models predict different dependencies. It is possible to identify at least three mechanisms for the loss of sound intensity in a homogeneous poro-elastic bottom:

- Inelastic losses in the sediment skeleton
- Viscous losses, associated with the relative movement of the interstitial fluid and the skeleton
- Losses due to volume scattering

These mechanisms give different dependencies of the absorption coefficient on frequency: from a proportionality to the square root of the frequency for the model of viscous losses to a proportionality to the fourth power of the frequency, associated with volume scattering, when the size of the scatterers is much less than the wavelength of the sound wave. It is obvious that the measured frequency dependence will represent some weighted combination of these mechanisms. Thus, site-specific studies are needed to explain the frequency dependence of the sound absorption in the bottom for a given shallow water region and for a given frequency band.

As a result of considering complex poro-elastic bottom models, various authors have proposed an exponential frequency dependence for the coefficient

$$\alpha(f) = \alpha_0 (f/f_0)^q. \tag{2.55}$$

Here, α is the determined sound absorption in the sea bottom. It is related to the bottom refractive index via $n_1^b = c(H)/[c_1(1 + i\alpha/2)]$, where c_1 is sound speed in the bottom, α_0 and f_0 are normalization coefficients, and q is the most important parameter, the exponential determining the frequency dependence. All these parameters depend on real, experimental conditions (i.e., the type of bottom). The

main parameter q has been the subject of significant interest for many authors who have measured it in diverse areas, mainly via the best fit between experimental and theoretical acoustical data. In Table 2.6 (courtesy of J. Holmes [J. Holmes et al. (2005)]), a compilation of the results from the different authors referenced above is presented. Intriguingly, the q parameter tends to cluster in a range of values between 1.5 and 2.0, the latter value being what the simple Biot theory would predict. It is thus obvious from the data that poro-elastic medium effects are important, and moreover that their exact explanation needs more than even the simpler forms of the Biot theory. We will examine this topic further in a later section. We will also look further at the measurements of q in a later chapter dedicated to inverse theory.

Two variants of the Biot theory that have attracted considerable recent attention in the underwater acoustics community are those by Buckingham (1997) and Pierce et al. (2004; Holmes et al. 2005). The former theory has been most extensively applied to higher frequency bottom dispersion data (with great success), whereas latter is tailored more toward low-frequency data.

2.11 Acoustics of Biological Objects in a Coastal Area

To a shallow water acoustician working at frequencies between 50 and 5,000 Hz, marine biology means pretty much two things: fish and marine mammals. We will disregard smaller flora or fauna as "weak effects" for this frequency range, and concentrate solely on these larger animals. Again, some basic references to start from might be (1) "Biological Oceanography" (Miller 2004) and (2) "Marine Mammals and Noise" (Richardson et al. 1995).

As to why we would consider fish and marine mammals, there are a variety of reasons. Starting with fish, it is well known that they can both significantly attenuate sound in forward propagation and backscatter sound, leading to significant volume reverberation. The former can lead to ambiguity and error in measurements of propagation loss and fluctuations (i.e., is it the ocean, the bottom, or the fish causing the signal?), whereas the latter can be a significant source of clutter in sonars. For many years, the effects of fish were ignored, both because they were intermittent/transient signals which were deemed *probably* not important in most transmission and reverberation experiments and sonar usages. (The emphasis is on the probably, because if a large fish school was present, the measurements could exhibit a substantial (unknown) error.) Also, the measurement of fish schools and classification of their members were just not advanced enough for the purposes of shallow water acoustic experiments, where one needs to know the fish distribution along an acoustic propagation path (be it one-way forward or two-way backscatter) during each transmission. The ship-borne surveys standardly used by fisheries and marine biologists (even with acoustic backscatter instruments) were just too slow, of low resolution, and space–time aliased to be of real value to shallow water acoustic work. However, this situation is probably changing, as we will discuss.

Table 2.6 Compilation of frequency-dependent attenuation results (courtesy of Holmes et al., unpublished manuscript 2005)

Reference	Frequency range (Hz)	Bottom type	Estimated critical angle (degrees)	Frequency dependent exponent (n) following af^n	Experimental technique[a]
Ingenito (1973)	400–750	Sand	19	1.75	M
Beebe et al. (1982)	100–600	Medium to coarse sand	29	1.76	TL
Beebe et al. (1982)	25–250	Coarse sand with gravel	35	1.57	TL
Zhou (1985)	80–800	Sand–silt–clay	19	1.84	M
Zhou et al. (1987)	100–1,000	Fine sand and silt	21	1.6	INV
Tatersall and Chizhik (1993)	100–8,000	Medium sand	24	2.0[b]	TL
Tappert and Yamamoto (1993)	50–800	Sand–silt–clay	19	2.0	TL
Carey and Evans (1998)	500–1,000	Sand–silt–clay	18	1.5	TL
Rozenfeld et al. (2001)	47–604	Sand–silt	23	1.8	TL
Peng et al. (2004)	100–500	Very fine sand	21	1.65	TL
Zhou et al. (2004a)	100–700	Very fine sand	22	1.63	INV
Knobles et al. (2004)	25–800	Fine sand	21	2.0	TL

[a]*M* Modal, *TL* Transmission Loss, *INV* Inversion

[b]Paper actually reports agreement with Biot theory, which gives $n = 2.0$ in the 100–1,000 Hz range

Another reason for considering fish in shallow water acoustics is to use shallow water acoustic techniques to *measure* the fish schools. The absorption and backscattering of sound by the fish can be used as signals in tomographic and beamforming imaging schemes, respectively (see Diachok et al. 2004; Makris et al. 2006). We will discuss these schemes in more detail shortly.

Turning to marine mammals, the population density of these animals is not so high that they will ever significantly attenuate or backscatter acoustic signals in our frequency range. However, the use of acoustic techniques to track these animals, for both population and behavior studies, is very valuable scientifically. Another reason that marine mammals are important for shallow water acoustics is because they are protected (under the US law) under the Marine Mammal Protection Act and, in cases of certain species, the Endangered Species Act. In order to perform shallow water acoustics with active sources, US researchers need to know where the animals are likely to be, and how the sounds being employed would affect them. Exposure levels need to be estimated, and based on this estimate, permits may or may not be required and issued. It is worth noting that estimating exposures and their effects is still a science/technology under development, as will be discussed further. Finally, the vocalizations of these animals can be considered a noise source for those using sonars for purposes other than marine mammal research.

Scattering and absorption of sound by fish. The study of the scattering and absorption of sound by fish is, at this point in time, a rather well-developed field. While there are certainly a number of open questions yet to be answered, there is also enough knowledge and technology available to enable a researcher to calculate what the scattering cross-section of sound is for a given frequency and species of fish (Clay and Medwin 1977). From a basic physics viewpoint, there are three salient regimes of scattering from a fish of size L (1) low-frequency, $L/\lambda \ll 1$, called the Rayleigh or "point scatterer" regime, (2) mid-frequency, $L/\lambda \approx 1$, called the resonant or "organ pipe" regime, and (3) high-frequency, $L/\lambda \gg 1$, called the geometric optics regime. The most important regime, for both scattering and absorption, is the resonant regime. At this frequency, the effect of the fish is greatest, often by several orders of magnitude over the other regimes. The resonance, it is well known, is due to the gas-filled swim bladder that most fishes have. This bladder accounts for ~90% of the sound scattering from the fish as a whole. The theory of this resonant scattering has evolved through the last few decades from that of a simple spherical gas bubble in water, roughly the size of the swim bladder, to that of an extended, irregular gas-bearing bladder encased in a fleshy housing that can be treated as an elastic medium with the correct shape and acoustic properties. Needless to say, calculations of the scattering cross-sections of fish with these more complicated geometries and material properties necessitate sophisticated scattering physics and computational codes – however, this is possible today, if one wants exact numbers. It can be argued (Diachok et al. 2004) that the "free bubble" approximation may be quite adequate for certain calculations (e.g., the resonant frequency); however, this probably should be examined on a case-by-case, species-by-species basis.

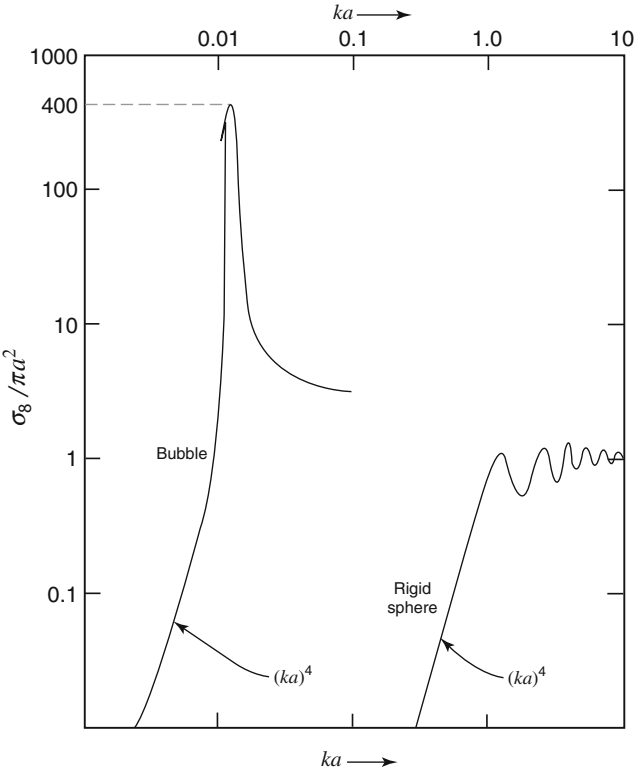


Fig. 2.28 Example of bubble and rigid sphere scattering cross-sections

It would be helpful to glance at what the cross-sections and attenuations are for fish, just to get an order-of-magnitude feel for them. In Fig. 2.28, we show (from Clay and Medwin 1977) a plot of the total scattering cross-section of a bubble compared to that of a rigid sphere. We use the dimensionless quantity *ka* instead of frequency in the ordinate, and the ratio of the total cross-section to the geometrical cross-section πa^2 in the abscissa, conventions widely used in scattering theory. One immediately sees that the sphere has a small total cross-section that peaks at (approximately) the geometric value, and a smooth transition from the Rayleigh scattering regime to the geometric regime. The bubble, on the other hand, has a whopping peak at the $ka = 1$ resonance, some 400 times bigger than the geometric value. It is obvious that resonance scattering is the main story for fish. We also note that the bubble scattering is approximately isotropic in direction so that the relations between the backscattering, forward scattering, and total cross-sections are simple. Thus, our lack of previous discussion of the directionality of the scattering.

The next part of the story, the attenuation, also shows sharp resonant effects, as seen in Fig. 2.29 from Diachok's work. In this figure, which does use real fish sizes and acoustic frequencies (not *ka* as before), we see that for a distribution of sardines

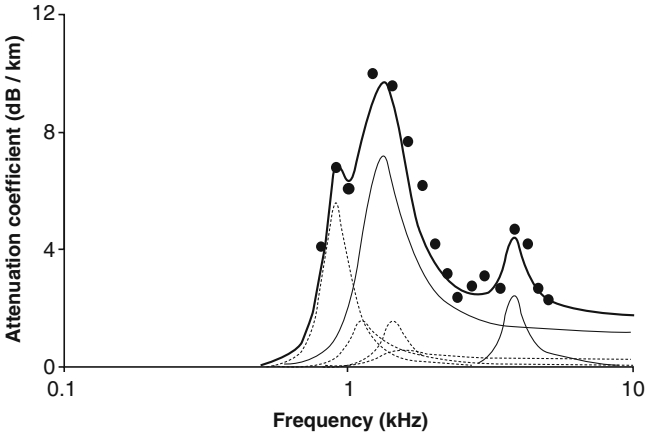


Fig. 2.29 Attenuation by fish vs. frequency, showing resonances (from Diachok)

(in age and size) ensonified at night, there is a distinct absorption peak at ~1.2 kHz, a wavelength that resonates with the dominant size fish in the distribution. The attenuations are seen to be substantial in the frequency band of interest to this book, and so if fish schools such as those measured by Diachok are present, biology needs to be part of propagation and scattering experiments, and the systems using them.

Population distributions of fish and surveying fish populations acoustically. The scattering and absorption cross-sections for fish are one part of the acoustic problem one needs to address. The distribution (in x, y, z, and t) of the fish and their species classification are another. In acoustic propagation studies, we need these quantities to factor out the effects of fish. Biologists and fisheries researchers are just as interested in these distributions and classifications for biological and economic reasons. To date, the standard method of surveying fish populations has been ship transects using acoustic echosounders ("fish finders") and tow nets to classify the species and give ground truth for the acoustic profiles. This method works to an extent, but it has low resolution and is severely space–time aliased. One might see the day–night migration of fish populations from the water column to the bottom, or get a rough idea of the dimensions of a fish school across the transect direction with these methods, but they still do not come close to a "snapshot" or series of snapshots of what is going on. Diachok has proposed using the resonant absorption of the fish to do an ocean CAT scan of fish populations, which he calls "resonance absorption tomography." However, the sorting out of fish attenuation from other ocean effects and the large number of slices needed to do tomography with good resolution make us think that this is an idea that is theoretically possible, but perhaps impractical in implementation. Recently, Makris et al. (2006) *were* able to produce a snapshot of fish shoals in the Atlantic using a pulsed, low-frequency, high power source array coupled with a very capable towed array receiver. The pulses echoed back strongly from

the fish schools, providing a "snapshot" with each pulse. The travel time of the pulse gave the range, and the steered beams the azimuth, producing beautiful 2D (x–y) time series views of the fish shoals over tens of kilometers with good resolution, and giving many new insights into their dimensions, structure, variability, biomass, etc. This combination of a low(er)-frequency pulsed source and a towed, steered array looking at backscatter seems to be the way to go in the future if one wishes to map fish populations effectively over large areas. We would make one suggestion as a possible future improvement of this method. As it stands, Makris' method requires large equipment and 2–3 ships to work (one for the source array, one for the towed receiver array, and one to net survey the area for ground truth as to species). Perhaps, by using several small AUVs equipped with mid-frequency (resonant) sources and directional receivers for this work, one could perform a survey equivalent to that using larger (and admittedly more range-capable) equipment. AUVs have already used high-frequency side-scan sonar and cameras to survey and classify fish populations at close ranges; so this is merely an extension and combination of the previous work by Makris and the AUV community.

Shallow water acoustics and marine mammals. Marine mammals enter into shallow water acoustics in (at least) five ways. First, one is interested in localizing marine mammals using their vocalizations. Tracking marine mammal "singers" with sound in the coastal waters that they frequent is, at this point in time, a well-worn path, but one which still has some interesting offshoots left. Second, one might regard marine mammal vocalizations as noise if using sonar for other purposes. The authors can testify to the amazingly interesting cacophony of sound one can hear in coastal waters (e.g., the Barents Sea, where we all have worked) due to seals, dolphins, and whales. This is a beautiful chorus to listen to, unless you are a sonar operator trying to listen to something else! Third, there is the ambient noise field in shallow water to consider, most especially that due to wind, waves, and shipping and pleasure craft. This acts as a hindrance to marine mammal communications. Next, there is the aspect of marine mammal protection via hazard mitigation – a new technology, but potentially important. And finally, there is the issue of regulation of active sources which are used by natural resource exploration vessels, science vessels, and the military.

Turning to the first topic, localization of vocalizing marine mammals in coastal waters using passive acoustic receivers, we would refer the reader to the article by Cato et al. in Medwin's "Sounds in the Sea" (2005) volume as a nice introduction, after which one will be comfortable in approaching the rather vast bioacoustic literature that exists on this topic. We would just note that while the basic acoustics and signal processing used for localization (time-delay cross-correlation, use of multipath and intensity information, etc.) has remained the same through the years, the technology being employed for this task has improved. AUVs with hydrophones, large-scale naval test ranges with *many* calibrated hydrophones, and even whale tags have been used to track whales and whale pods acoustically, with ever-increasing success. Being able to locate and track marine mammals (and fish) is one of the hardest tasks in marine biology, and passive acoustics is a tool that has provided some measure of success.

As to the sounds that the marine mammals make, many of these are in the range of frequencies of interest to us here (50–5,000 Hz), and many are quite loud – the mammals often need to communicate over many kilometers in shallow water, and evolution has tailored their source levels and frequencies to meet this need. For instance, baleen whales (e.g., finbacks and humpbacks) typically vocalize under 1 kHz and have source levels in the 150–190 dB re 1 μPa-m range, similar to source levels often used for research in shallow water. Odontocete whales often vocalize in our "medium frequency" (1–5 kHz) range. For example, killer whales emit pulses from ~1 to 6 kHz, with peak levels of 160 dB re 1 μPa-m. There is much more to this topic (as always), and we would again refer the interested reader to the volume "Marine mammals and noise" by Richardson et al. (1995) as a basic reference to start with.

The third piece of shallow water acoustics of interest to marine mammal studies is the "general ambient noise field," i.e., the background susurrus due to wind, waves, distant shipping, drilling platforms, pleasure craft, and the like. However, the word "din" or "racket" is perhaps preferable to "susurrus," as the ocean is a noisy place – often due to natural causes, but increasingly due to anthropogenic noise. It has been estimated that the low-frequency ambient noise in the Northern Hemisphere has increased by 10–20 dB over the 10–1,000-Hz band (a number that is rather hard to make exact, due to undersampling issues) solely due to anthropogenic noise, a rather startling finding. (The 2003 National Research Council volume on "Ocean noise and marine mammals" makes an excellent starting point for such an overview.) Whatever the exact number, it is clear that human activities have added to the shallow water noise field (especially, since most anthropogenic maritime activity is coastal) and that this has affected marine mammals. Again, we will forego much detail here in favor of references to a well-established literature.

Mitigation is another active area of acoustics that intersects with marine mammals and shallow water. Two typical mitigation issues that come up are (1) avoidance of ship strikes to marine mammals in shallow water and (2) strategies for "ramping up" louder active sources that could affect marine mammals in their immediate vicinity. Regarding the former topic, there does not seem to be any low- or medium-frequency signal that a ship can send to a surfaced marine mammal to say "Danger! Get out of the way!" at least at present. Warning these animals of a pending collision would be a very useful thing, but unfortunately right whales got their name by being absolutely unresponsive to human activity in their vicinity, which made them the "right whale" to hunt in the heyday of the whaling industry. A more useful tool is the forward-looking obstacle avoidance sonar, which can be purchased commercially. This is higher frequency equipment (e.g., one can look at the system by FarSounder, Inc.) and so is a bit beyond the purview of this book.

Finally, there is the issue of estimating the exposure of marine mammals to low- and medium-frequency sound in shallow water. This has been a major research issue, both from the point of view of noise models and databases (again, see the National Academy 2003 reportsas a starting point) and also from the point of estimating the levels from individual military, industrial, and research sources.

Looking at models and databases, the recent Effects of Sound on the Marine Environment (ESME) model created by the Office of Naval Research is a good

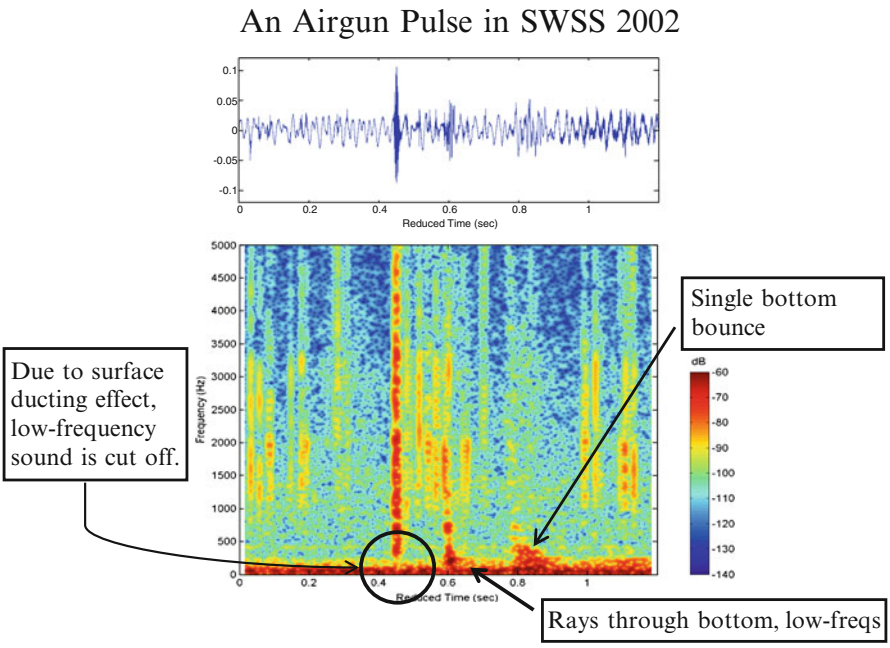


Fig. 2.30 Spectrogram showing energy in acoustic band from seismic source (from DeReuter et al.)

example of an interdisciplinary model (acoustics, biology, physical oceanography, and marine geology) that attempts to calculate exposures and their effects (from both ambient noise and discrete sources) on marine mammals using the latest research results as much as possible (see the IEEE Journal of Oceanic Engineering Special Issue on this topic in 2004 for detailed papers). Moreover, this model has also inspired more research in the areas that were deemed "underdeveloped" for that purpose – a truthful admission that such model outputs are estimates that can be improved.

As an example of direct shallow water research that deals with marine mammal exposures from discrete sources, we will take the work by DeRuiter et al. (2006). In her paper, DeRuiter showed that finescale coastal oceanography effects (in this case, a near-surface duct) could produce some exposure of marine mammals at the surface to the higher frequency components of a seismic airgun signal (see Fig. 2.30). This somewhat surprised the seismic community, which did not worry about detailed oceanography very much – but it was less of a surprise to coastal, shallow water acousticians, who routinely see such effects. Indeed, much of the material in the rest of this book is concerned with just such effects.

We will leave the topic of marine mammals for now, with the realization that all we have done is to point out some major directions in a huge field. Like all the sciences that shallow water acoustics interacts with, marine biology is not only a vast one, but also an important one for acoustic practitioners.



http://www.springer.com/978-1-4419-9776-0

Fundamentals of Shallow Water Acoustics
Katsnelson, B.; Petnikov, V.; Lynch, J.F.
2012, XVI, 540 p., Hardcover
ISBN: 978-1-4419-9776-0